

Mono-/Bimetallic Neutral Iridium(III) Complexes Bearing Diketopyrrolopyrrole-Substituted N-Heterocyclic Carbene Ligands: Synthesis and Photophysics

Wan Xu, Levi Lystrom, Yanxiong Pan, Xinyang Sun, Salim A. Thomas, Svetlana V. Kilina, Zhongyu Yang, Hua Wang, Erik K. Hobbie, and Wenfang Sun*

Cite This: *Inorg. Chem.* 2021, 60, 15278–15290

Read Online

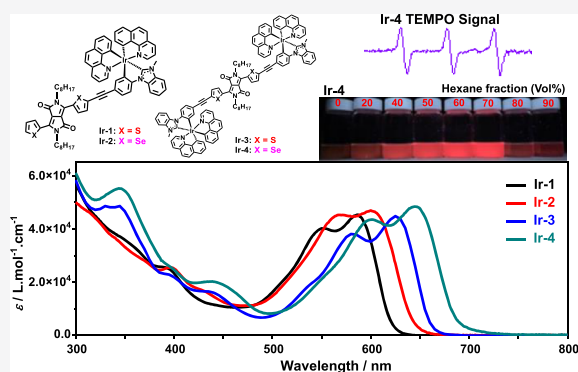
ACCESS |

Metrics & More

Article Recommendations

Supporting Information

ABSTRACT: The synthesis and photophysics (UV–vis absorption, emission, and transient absorption) of four neutral heteroleptic cyclometalated iridium(III) complexes (**Ir-1**–**Ir-4**) incorporating thiophene/selenophene-diketopyrrolopyrrole (DPP)-substituted N-heterocyclic carbene (NHC) ancillary ligands are reported. The effects of thiophene versus selenophene substitution on DPP and bis- versus monoiridium(III) complexation on the photophysics of these complexes were systematically investigated via spectroscopic techniques and density functional theory calculations. All complexes exhibited strong vibronically resolved absorption in the regions of 500–700 nm and fluorescence at 600–770 nm, and both are predominantly originated from the DPP-NHC ligand. Complexation induced a pronounced red shift of this low-energy absorption band and the fluorescence band with respect to their corresponding ligands due to the improved planarity and extended π -conjugation in the DPP-NHC ligand. Replacing the thiophene units by selenophenes and/or biscomplexation led to the red-shifted absorption and fluorescence spectra, accompanied by the reduced fluorescence lifetime and quantum yield and enhanced population of the triplet excited states, as reflected by the stronger triplet excited-state absorption and singlet oxygen generation.



INTRODUCTION

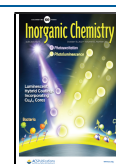
Developing molecules that strongly absorb and/or emit in the far-red to near-infrared (NIR) regions has aroused significant attention due to their wide applications on night-vision devices, optoelectronics, heat shielding, information security displays, phototherapy, bioimaging, and so forth.^{1–9} Particularly, far-red/NIR-absorbing molecules are desirable photosensitizers for photodynamic and/or photothermal therapy because light in these spectral regions can penetrate tissue deeper.^{10–12} For the same reason, far-red/NIR-emitting molecules are attractive for bioimaging applications.^{4,5,9} Far-red/NIR-absorbing molecules are also desired for dye-sensitized solar cells (DSSCs)⁶ or triplet–triplet annihilation upconversion (TTA-UC) applications¹³ because solar light has significant far-red/NIR components. To date, most of the far-red/NIR-absorbing molecules are organic molecules with an extended π -conjugation.^{1,2,4–7,9} Studies on far-red/NIR-absorbing transition-metal complexes have been rare.^{14–24}

Unlike many of the unstable π -conjugated organic far-red/NIR molecules, some transition-metal complexes such as metallophthalocyanines and metallophthalocyanines are highly stable and possess rich photophysical properties.^{22,23} Especially for heavy transition-metal-containing complexes, the heavy-atom-enhanced intersystem crossing (ISC) facilitates the

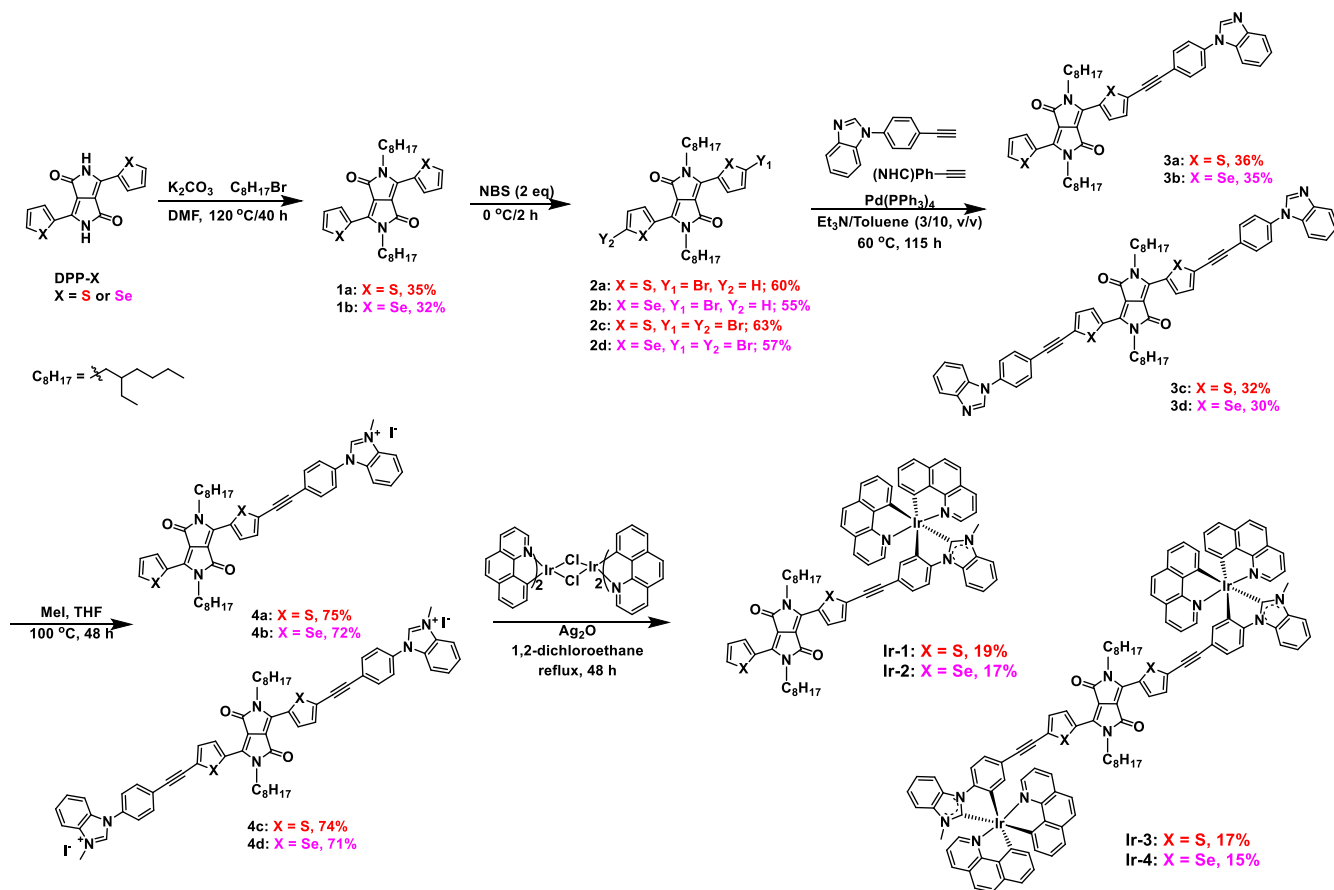
population of the triplet excited state, which is a desirable feature for photosensitizers employed for PDT or TTA-UC applications.^{14–21} In recent years, Ir(III) complexes have emerged as a new platform for theranostic PDT applications.^{24–28} Ir(III) possesses stronger ligand field strengths than Ru(II), pushing the nonradiative deactivating d–d state to a much higher energy than the ligand-based $^3\pi, \pi^*$ or metal-to-ligand charge transfer ($^3\text{MLCT}$) states and thus generating a long-lived $^3\pi, \pi^*$ or $^3\text{MLCT}$ state for the Ir(III) complex compared to the corresponding Ru(II) complex. We have demonstrated that tricationic Ir(III) complexes exhibited >1 order of magnitude longer lowest-energy triplet excited-state (T_1) lifetimes compared to their Ru(II) counterparts bearing the same set of diimine ligands.²⁹ The bisterpyridyl Ir(III) complexes also possessed a much longer-lived T_1 state than their Ru(II) counterparts.^{30,31} The Ir(III) ion has one of the

Received: June 18, 2021

Published: September 28, 2021



Scheme 1. Structures and Synthetic Routes for Complexes Ir-1–Ir-4



largest spin–orbit coupling (SOC) constants among all of the transition metals,³² facilitating the T_1 state formation via ISC. However, most of the currently studied Ir(III) complexes mainly absorb light in the UV to blue spectral regions, wavelengths of lesser interest for PDT because of their shallow tissue penetration due to tissue scattering and absorption.⁴ Efforts in red-shifting the absorption of the Ir(III) complexes to far-red/NIR spectral regions have been quite limited.^{14,17,20,21,24}

To date, two of the reported red/NIR-absorbing Ir(III) complexes bear the styryl-BODIPY (boron dipyrromethene difluoride) or cyanine motif.^{20,21} Although the absorption of the styryl-BODIPY-containing complexes was red-shifted to 606–729 nm and their T_1 states were long-lived (~ 31 – 157 μ s), the in vitro PDT effects of these complexes were quite weak, with high dark toxicity (inhibitory concentration to reduce the cell viability to 50%, IC_{50} = 8.16– 16.70 μ M) and minimal phototherapeutic indices (PIs < 4) upon 635 nm excitation.²⁰ In addition, these complexes readily decompose upon light irradiation. For the Ir(III)–cyanine complex nanoparticles, although it showed a significant in vivo PDT effect upon 808 nm irradiation, its singlet oxygen generation efficiency was quite low (4.36%).²¹ To overcome these shortcomings, more robust red/NIR light-harvesting chromophores are needed.

Diketopyrrolopyrrole (DPP) and its derivatives are promising candidates because of their strong visible-light absorption, better thermal- and photostability, and ease of structural modifications.^{33–35} DPP derivatives and their polymeric materials have been explored for applications in photo-

refractive materials,³⁶ fluorescence sensors,³⁷ light-emitting diodes,³⁸ photovoltaics,³⁹ and DSSC.^{34,40} It was also reported that the optoelectric properties of DPP derivatives could be easily tuned by altering the aromatic substituents appended to the DPP, especially chalcogenophene substitution bathochromically shifted the absorption to longer wavelengths.^{35,41} Incorporation of transition-metal complexes, such as Pt(II) and/or Ir(III) complexes, to DPP derivatives via covalent linkage not only enhanced the ISC to the triplet state of the DPP derivatives but also extended the π -conjugation of the DPP derivatives and induced further red shifts.^{19,42,43} Meanwhile, a long-lived ligand-localized T_1 state was retained, which was able to generate singlet oxygen as demonstrated by dinuclear cationic Ir(III) complexes bearing the DPP bridging linkage.⁴²

Our group has extensively explored a variety of Ir(III) complexes for PDT, which include a series of neutral Ir(III) complexes with the BODIPY-substituted N-heterocyclic carbene (NHC) ligand.^{17,31,44–48} Although these complexes exhibited strong in vitro PDT effects, the absorption of these complexes was limited to the green spectral regions. Inspired by this result and by the advantages of the DPP derivatives, herein we incorporated DPP derivatives to the NHC-containing neutral Ir(III) complexes via $C\equiv C$ triplet bond(s) to red-shift the absorption of the Ir(III) complexes to the orange/red spectral regions while imparting internal heavy atoms (i.e., S or Se from the thiophene or selenophene rings, respectively) to enhance the triplet excited-state population. The structures of the synthesized complexes Ir-1–Ir-4 are presented in Scheme 1. Both mononuclear and

dinuclear complexes are synthesized to assess the effects of additional Ir(III) complexation on the ground- and excited-state properties. Different chalcogenophenes, that is, thiophenes or selenophenes, were attached to DPP to further red-shift the absorption and induce additional heavier atom(s). It has been reported that the larger size of the selenium (Se) atom reduced the overlap of the Se orbitals with the π -orbitals of the carbon skeleton, leading to increased quinoidal contribution and double-bond character.^{49,50} The shorter C–C bonds from the significantly contributing quinoid structures resulted in a red shift in the absorption of selenophene-containing compounds.⁵¹ Moreover, the heavier Se atom could facilitate the formation of the triplet excited state because transition-metal complexes with a π -expensive ligand could have a small SOC due to the reduced contributions of metal d -orbitals to the frontier molecular orbitals of the complexes.⁵² The neutral Ir(III) complex rather than the cationic complex was selected for study in this work because the hydrophobicity of the neutral complexes could facilitate their encapsulation into self-assembled micelles for future PDT studies. Nonetheless, the aim of this work is to understand the structure–property correlations in these DPP-containing Ir(III) complexes.

EXPERIMENTAL SECTION

Synthesis and Characterizations. All chemicals and solvents were purchased from Sigma-Aldrich, Alfa Aesar, or VWR International and used as received. Silica gels (60 Å, 230–400 mesh) used for column chromatography were purchased from Sorbent Technology. The intermediate compounds and ligands were characterized by ¹H NMR spectroscopy, while the Ir(III) complexes were characterized by ¹H NMR, HRMS, and elemental analysis. ¹H NMR spectra were recorded on a Varian Oxford-400 or a Bruker 400 MHz spectrometer in CDCl₃ or DMSO-*d*₆, with tetramethylsilane as the internal standard. A Bruker BioTOF III mass spectrometer was used for ESI-HRMS analyses. Elemental analyses were carried out by NuMega Resonance Laboratories, Inc., in San Diego, California.

Benzo[*h*]quinoline (C^NN ligand) was obtained from Alfa-Aesar and its Ir(III) μ -chloro-bridged dimers [Ir(C^NN)₂Cl]₂ were synthesized according to the literature procedure.⁵³ Compounds 3,6-bis-(thiophenyl)-1,4(2*H*,5*H*)-diketopyrrolo[3,4-*c*]pyrrole (DPP-S),⁵⁴ 3,6-bis(selenophenyl)-1,4(2*H*,5*H*)-diketopyrrolo[3,4-*c*]pyrrole (DPP-Se),^{35,55} 2,5-bis(2-ethylhexyl)-3,6-di(thiophen-2-yl)-pyrrolo[3,4-*c*]pyrrole-1,4(2*H*,5*H*)-dione (1a),⁵⁶ 2,5-bis(2-ethylhexyl)-3,6-di(selenophen-2-yl)-pyrrolo[3,4-*c*]pyrrole-1,4(2*H*,5*H*)-dione (1b),^{57,58} 3-(5-bromothiophen-2-yl)-2,5-bis(2-ethylhexyl)-2,5-dihydro-6-(thiophen-2-yl)-pyrrolo[3,4-*c*]pyrrole-1,4(2*H*,5*H*)-dione (2a),^{59,60} 3-(5-bromoselenophen-2-yl)-2,5-bis(2-ethylhexyl)-2,5-dihydro-6-(selenophen-2-yl)-pyrrolo[3,4-*c*]pyrrole-1,4(2*H*,5*H*)-dione (2b),⁵⁸ 3,6-bis(5-bromothiophen-2-yl)-2,5-bis(2-ethylhexyl)-pyrrolo[3,4-*c*]pyrrole-1,4(2*H*,5*H*)-dione (2c),^{56,59,60} and 3,6-bis(5-bromoselenophen-2-yl)-2,5-bis(2-ethylhexyl)-pyrrolo[3,4-*c*]pyrrole-1,4(2*H*,5*H*)-dione (2d)⁵⁸ were synthesized following the reported procedures. The synthetic procedures and characterization data for 3a–3d, 4a–4d, and Ir-1–Ir-4 are reported below, and the ¹H NMR, ¹³C NMR, and HRMS spectra of Ir-1–Ir-4 are provided in Supporting Information, Figures S1–S3.

General Synthetic Procedure for 3a–3d. To a degassed solution of compounds 2a–2d (1 equiv, 0.99 mmol) and (NHC)Ph \equiv (1.05 equiv, 1.04 mmol for synthesizing 3a and 3b and 2.10 equiv, 2.08 mmol for synthesizing 3c and 3d) in toluene (20 mL)/triethylamine (6 mL) was added Pd(PPh₃)₄ (0.03 equiv, 0.03 mmol for synthesizing 3a and 3b and 0.06 equiv, 0.06 mmol for synthesizing 3c and 3d). The reaction mixture was heated to 60 °C for 115 h under a nitrogen atmosphere. The reaction mixture was then cooled to room temperature (rt) and concentrated under reduced pressure. The residue was washed with water (30 mL) and brine (30 mL),

respectively, and then extracted with CH₂Cl₂ (3 \times 10 mL). The CH₂Cl₂ fractions were combined and washed with water (3 \times 30 mL) and then dried over MgSO₄. After removal of the solvent, the crude product was purified by using silica gel column chromatography [CH₂Cl₂/acetone = 10:1 (v/v) for 3a and 3b and CH₂Cl₂/acetone = 5:1 (v/v) for 3c and 3d] to obtain the product.

3a. A red powder (0.26 g, 36%) was obtained. ¹H NMR (400 MHz, CDCl₃): δ (ppm) 8.95 (d, *J* = 4.0 Hz, 1H), 8.87 (d, *J* = 4.0 Hz, 1H), 8.15 (s, 1H), 7.91–7.89 (m, 1H), 7.75 (d, *J* = 8.0 Hz, 2H), 7.66 (d, *J* = 4.0 Hz, 1H), 7.60–7.55 (m, 3H), 7.44 (d, *J* = 4.0 Hz, 1H), 7.38–7.36 (m, 2H), 7.30–7.27 (m, 1H), 4.06–4.01 (m, 4H), 1.91–1.87 (m, 2H), 1.39–1.24 (m, 16H), and 0.93–0.84 (m, 12H). ¹³C NMR (400 MHz, CDCl₃): δ (ppm) 161.70, 161.55, 142.96, 141.69, 140.97, 139.01, 136.23, 135.76, 135.06, 133.37, 133.27, 133.07, 131.20, 131.01, 129.74, 128.55, 127.43, 124.38, 123.88, 123.59, 122.41, 120.46, 110.65, 108.96, 108.03, 95.93, 83.99, 46.05, 45.97, 39.17, 39.09, 30.21, 30.16, 28.36, 23.58, 23.55, 23.08, 14.07, 14.04, 10.52, and 10.49. ESI-HRMS (*m/z*): calcd for [C₄₅H₄₈N₄O₂S₂]⁺, 741.3297; found, 741.3294.

3b. A purplish-red powder (0.29 g, 35%) was obtained. ¹H NMR (400 MHz, CDCl₃): δ (ppm) 8.89 (d, *J* = 4.0 Hz, 1H), 8.77 (d, *J* = 4.0 Hz, 1H), 8.43 (d, *J* = 8.0 Hz, 1H), 8.15 (s, 1H), 7.74 (d, *J* = 8.0 Hz, 2H), 7.60–7.55 (m, 4H), 7.50 (t, *J* = 4.0 Hz, 2H), 7.38–7.36 (m, 2H), 3.99–3.96 (m, 4H), 1.92–1.87 (m, 2H), 1.37–1.26 (m, 16H), and 0.92–0.84 (m, 12H). ¹³C NMR (400 MHz, CDCl₃): δ (ppm) 161.83, 161.70, 143.17, 142.64, 141.73, 140.80, 137.54, 137.04, 136.22, 136.16, 135.94, 135.55, 133.92, 133.16, 132.63, 130.90, 124.33, 123.87, 123.52, 122.64, 120.51, 110.63, 109.08, 108.15, 98.30, 86.25, 46.03, 45.89, 39.12, 39.03, 30.24, 28.35, 28.33, 23.62, 23.60, 23.08, 14.05, 10.52, and 10.47. ESI-HRMS (*m/z*): calcd for [C₄₅H₄₈N₄O₂Se₂]⁺, 837.2197; found, 837.2185.

3c. A purplish-red powder (0.31 g, 32%) was obtained. ¹H NMR (400 MHz, CDCl₃): δ (ppm) 8.92 (d, *J* = 4.0 Hz, 2H), 8.16 (s, 2H), 7.93–7.89 (m, 2H), 7.76 (d, *J* = 8.0 Hz, 4H), 7.60–7.56 (m, 6H), 7.45 (d, *J* = 4.0 Hz, 2H), 7.39–7.37 (m, 4H), 4.06–4.04 (m, 4H), 1.95–1.90 (m, 2H), 1.43–1.26 (m, 16H), and 0.95–0.88 (m, 12H). ¹³C NMR (400 MHz, CDCl₃): δ (ppm) 161.54, 141.52, 139.55, 136.10, 135.52, 133.47, 133.33, 132.07, 131.07, 127.90, 124.60, 123.97, 123.87, 122.55, 120.25, 110.75, 109.09, 96.18, 84.03, 46.16, 39.18, 30.17, 28.34, 23.58, 23.09, 14.08, and 10.50. ESI-HRMS (*m/z*): calcd for [C₆₀H₅₆N₆O₂S₂ + 2H]⁺, 959.4141; found, 959.4121.

3d. A purplish-red powder (0.31 g, 30%) was obtained. ¹H NMR (400 MHz, CDCl₃): δ (ppm) 8.82 (d, *J* = 4.0 Hz, 2H), 8.16 (s, 2H), 7.91–7.89 (m, 2H), 7.75 (d, *J* = 8.0 Hz, 4H), 7.62–7.56 (m, 8H), 7.39–7.36 (m, 4H), 4.01–3.98 (m, 4H), 1.95–1.91 (m, 2H), 1.42–1.26 (m, 16H), and 0.94–0.87 (m, 12H). ¹³C NMR (400 MHz, CDCl₃): δ (ppm) 161.69, 141.55, 141.22, 136.59, 136.09, 135.80, 135.67, 133.21, 133.11, 124.54, 123.96, 123.79, 122.77, 120.31, 110.74, 109.22, 98.58, 86.30, 46.14, 39.15, 30.23, 28.32, 23.62, 23.09, 14.06, and 10.50. ESI-HRMS (*m/z*): calcd for [C₆₀H₅₆N₆O₂Se₂]⁺, 1053.2889; found, 1053.2878.

General Synthetic Procedure for 4a–4d. Compounds 3a–3d (0.94 mmol) and iodomethane [0.09 mL (1.41 mmol) for synthesizing 4a and 4b and 0.18 mL (2.82 mmol) for synthesizing 4c and 4d] were dissolved in 20 mL of degassed tetrahydrofuran (THF) in a 100 mL pressure tube and heated to 100 °C for 48 h. After the reaction mixture was cooled to rt, 5 mL of hexane was added. The mixture was centrifuged, and the solid was filtered out and dried in vacuo to obtain a black solid. The black solid was dissolved in 10 mL of CH₂Cl₂ and washed with water (3 \times 30 mL), and the combined organic fractions were dried over MgSO₄. After removal of the solvent, the residue was purified by using silica gel column chromatography [CH₃OH/acetone = 1:3 (v/v) for 4a and 4b and CH₃OH/acetone = 1:1 (v/v) for 4c and 4d] to yield the product.

4a. A purplish-red powder was obtained (0.62 g, 75%). ¹H NMR (400 MHz, CDCl₃): δ (ppm) 11.11 (s, 1H), 8.94 (d, *J* = 4.0 Hz, 1H), 8.84 (d, *J* = 4.0 Hz, 1H), 7.98 (d, *J* = 12.0 Hz, 2H), 7.83 (d, *J* = 8.0 Hz, 3H), 7.78–7.72 (m, 3H), 7.65 (d, *J* = 4.0 Hz, 1H), 7.46 (d, *J* = 4.0 Hz, 1H), 7.28–7.27 (m, 1H), 4.46 (s, 3H), 4.05–4.01 (m, 4H), 1.89–1.86 (m, 2H), 1.43–1.25 (m, 16H), and 0.93–0.84 (m, 12H).

^{13}C NMR (400 MHz, CDCl_3): δ (ppm) 161.66, 161.48, 142.30, 141.08, 138.83, 135.83, 134.93, 133.81, 133.63, 132.70, 132.28, 131.61, 131.06, 130.94, 130.75, 130.63, 129.72, 128.54, 128.16, 127.94, 126.87, 125.36, 125.19, 113.55, 113.41, 109.04, 107.98, 95.14, 85.36, 46.05, 45.97, 39.14, 39.07, 34.79, 30.22, 30.16, 28.35, 23.58, 23.54, 23.07, 14.08, 14.04, 10.52, and 10.48. ESI-HRMS (m/z): calcd for $[\text{C}_{46}\text{H}_{51}\text{N}_4\text{O}_2\text{S}_2 - \text{H}]^+$, 755.3453; found, 755.3439.

4b. A purplish-red powder was obtained (0.65 g, 72%). ^1H NMR (400 MHz, CDCl_3): δ (ppm) 11.14 (s, 1H), 8.89 (d, $J = 4.0$ Hz, 1H), 8.75 (d, $J = 4.0$ Hz, 1H), 8.41 (d, $J = 4.0$ Hz, 1H), 7.97 (d, $J = 8.0$ Hz, 2H), 7.82–7.70 (m, 6H), 7.63 (d, $J = 4.0$ Hz, 1H), 7.50–7.48 (m, 1H), 4.46 (s, 3H), 4.00–3.96 (m, 4H), 1.92–1.87 (m, 2H), 1.38–1.24 (m, 16H), and 0.92–0.84 (m, 12H). ^{13}C NMR (400 MHz, CDCl_3): δ (ppm) 161.83, 161.66, 142.31, 140.68, 137.61, 137.12, 136.46, 136.07, 133.90, 133.81, 133.56, 133.23, 132.54, 132.27, 132.25, 131.82, 130.99, 130.91, 128.23, 128.22, 128.00, 125.73, 125.15, 125.04, 113.61, 113.34, 109.18, 108.13, 97.36, 88.45, 46.04, 45.90, 39.11, 39.01, 34.72, 30.23, 28.35, 28.33, 23.62, 23.59, 23.08, 14.06, 14.04, 10.52, and 10.47. ESI-HRMS (m/z): calcd for $[\text{C}_{46}\text{H}_{51}\text{N}_4\text{O}_2\text{Se}_2 - \text{H}]^+$, 851.2354; found, 851.2350.

4c. A purplish-red powder was obtained (0.86 g, 74%). ^1H NMR ($\text{DMSO}-d_6$, 400 MHz): δ (ppm) 10.19 (s, 2H), 8.78 (d, $J = 4.0$ Hz, 2H), 8.17 (d, $J = 8.0$ Hz, 2H), 8.01 (d, $J = 8.0$ Hz, 4H), 7.94–7.91 (m, 4H), 7.83–7.74 (m, 8H), 4.19 (s, 6H), 4.00–3.80 (m, 4H), 1.79–1.75 (m, 2H), 1.34–1.20 (m, 16H), and 0.88–0.81 (m, 12H). ^{13}C NMR (400 MHz, $\text{DMSO}-d_6$): δ (ppm) 161.12, 143.75, 139.19, 135.23, 134.91, 134.16, 133.84, 132.39, 131.29, 131.13, 128.02, 127.54, 127.19, 126.09, 123.64, 114.51, 113.88, 108.84, 97.90, 84.43, 45.76, 38.90, 34.05, 30.00, 28.19, 23.67, 22.82, 14.26, and 10.74. ESI-HRMS (m/z): calcd for $[\text{C}_{62}\text{H}_{62}\text{N}_6\text{O}_2\text{S}_2 - 2\text{H}]^{2+}$, 493.2188; found, 493.2177.

4d. A purplish-red powder was obtained (0.89 g, 71%). ^1H NMR ($\text{DMSO}-d_6$, 400 MHz): δ (ppm) 10.19 (s, 2H), 8.72 (d, $J = 4.0$ Hz, 2H), 8.17 (d, $J = 8.0$ Hz, 2H), 8.01 (d, $J = 8.0$ Hz, 4H), 7.93 (d, $J = 12.0$ Hz, 4H), 7.89 (d, $J = 4.0$ Hz, 2H), 7.83–7.74 (m, 6H), 4.19 (s, 6H), 3.98–3.96 (m, 4H), 1.78–1.75 (m, 2H), 1.27–1.19 (m, 16H), and 0.87–0.80 (m, 12H). ^{13}C NMR (400 MHz, $\text{DMSO}-d_6$): δ (ppm) 161.32, 143.76, 140.89, 137.11, 136.67, 136.34, 134.02, 133.70, 132.46, 132.39, 131.12, 128.01, 127.53, 126.04, 124.06, 114.52, 113.90, 109.06, 98.80, 87.02, 45.71, 38.80, 34.05, 29.97, 28.13, 23.67, 22.84, 14.24, and 10.75. ESI-HRMS (m/z): calcd for $[\text{C}_{62}\text{H}_{62}\text{N}_6\text{O}_2\text{Se}_2 - 2\text{H}]^{2+}$, 541.1641; found, 541.1648.

General Synthetic Procedure for Ir-1–Ir-4. Compounds **4a–4d** (0.23 mmol), Ag_2O [0.10 g (0.46 mmol)] for synthesizing **Ir-1** and **Ir-2** and 0.20 g (0.92 mmol) for synthesizing **Ir-3** and **Ir-4**, and $[\text{Ir}(\text{benzo}[\text{H}]\text{quinoline})_2(\mu\text{-Cl})_2]$ [0.14 g (0.11 mmol)] for synthesizing **Ir-1** and **Ir-2** and 0.29 g (0.22 mmol) for synthesizing **Ir-3** and **Ir-4** were dissolved in 20 mL of 1,2-dichloroethane, and the mixture was degassed with nitrogen. The reaction mixture was heated at 90 °C for 48 h in the dark and then cooled to rt. The mixture was extracted with CH_2Cl_2 (3×10 mL), and the organic phase was washed with water (3×30 mL). The combined organic fractions were dried over MgSO_4 , and the solvent was removed. The residue was purified by using silica gel column chromatography [hexane/ $\text{CH}_2\text{Cl}_2 = 1:1$ (v/v) for **Ir-1** and **Ir-2** and hexane/ $\text{CH}_2\text{Cl}_2 = 1:2$ (v/v) for **Ir-3** and **Ir-4**] to obtain the product.

Ir-1. A purplish-red solid was obtained (50 mg, 15%). ^1H NMR (400 MHz, CDCl_3): δ (ppm) 8.88 (d, $J = 4.0$ Hz, 1H), 8.40 (d, $J = 4.0$ Hz, 1H), 8.26 (d, $J = 8.0$ Hz, 1H), 8.21 (d, $J = 8.0$ Hz, 1H), 8.06 (t, $J = 8.0$ Hz, 2H), 7.90 (d, $J = 8.0$ Hz, 1H), 7.81–7.76 (dd, $J = 8.0$, 12.0 Hz, 2H), 7.61 (d, $J = 8.0$ Hz, 1H), 7.55 (d, $J = 8.0$ Hz, 2H), 7.40–7.32 (m, 3H), 7.31–7.27 (m, 4H), 7.25–7.15 (m, 4H), 7.13–7.05 (m, 3H), 6.66 (d, $J = 8.0$ Hz, 1H), 6.36 (d, $J = 8.0$ Hz, 1H), 4.04–3.96 (m, 4H), 3.26 (s, 3H), 1.88–1.84 (m, 2H), 1.37–1.26 (m, 16H), and 0.89–0.83 (m, 12H). ^{13}C NMR (400 MHz, CDCl_3): δ (ppm) 189.68, 169.10, 168.72, 161.76, 161.59, 159.91, 158.79, 155.47, 151.89, 151.60, 150.50, 142.12, 141.51, 140.68, 139.99, 139.93, 136.71, 135.75, 135.22, 134.35, 134.30, 134.21, 133.68, 132.91, 132.18, 130.44, 130.34, 130.11, 130.00, 129.92, 129.58, 129.56, 129.08, 128.44, 127.67, 127.05, 126.79, 126.49, 123.47,

123.00, 122.80, 122.49, 121.04, 120.96, 118.26, 118.06, 111.77, 111.61, 110.21, 108.20, 100.59, 81.15, 68.18, 46.03, 45.92, 39.09, 39.04, 33.79, 30.23, 30.09, 29.73, 28.37, 28.26, 23.54, 23.50, 23.07, 14.07, 14.04, and 10.49. ESI-HRMS (m/z): calcd for $[\text{C}_{72}\text{H}_{65}\text{N}_6\text{O}_2\text{S}_2\text{Ir}]^+$, 1302.4243; found, 1302.4216. Anal. Calcd (%) for $\text{C}_{72}\text{H}_{65}\text{IrN}_6\text{O}_2\text{S}_2 \cdot \text{C}_6\text{H}_{14} \cdot \text{C}_3\text{H}_6\text{O}$: C, 67.24; H, 5.92; and N, 5.81. Found: C, 67.05; H, 5.94; and N, 5.52.

Ir-2. A purplish-red solid was obtained (54 mg, 16%). ^1H NMR (400 MHz, CDCl_3): δ (ppm) 8.82 (d, $J = 4.0$ Hz, 1H), 8.40 (d, $J = 12.0$ Hz, 1H), 8.37 (d, $J = 4.0$ Hz, 1H), 8.26 (d, $J = 8.0$ Hz, 1H), 8.22 (d, $J = 8.0$ Hz, 1H), 8.06 (t, $J = 8.0$ Hz, 2H), 7.90 (d, $J = 8.0$ Hz, 1H), 7.79 (dd, $J = 8.0$, 12.0 Hz, 2H), 7.56–7.52 (m, 2H), 7.49–7.46 (m, 1H), 7.41–7.36 (m, 3H), 7.34–7.27 (m, 3H), 7.24–7.15 (m, 4H), 7.13–7.07 (m, 2H), 7.05 (d, $J = 4.0$ Hz, 1H), 6.67 (d, $J = 4.0$ Hz, 1H), 6.36 (d, $J = 8.0$ Hz, 1H), 3.99–3.90 (m, 4H), 3.26 (s, 3H), 1.91–1.83 (m, 2H), 1.36–1.23 (m, 16H), and 0.88–0.83 (m, 12H). ^{13}C NMR (400 MHz, CDCl_3): δ (ppm) 189.65, 169.11, 168.75, 161.89, 161.73, 159.91, 158.78, 155.48, 151.91, 151.60, 150.50, 142.00, 141.74, 141.70, 141.52, 140.69, 137.14, 136.93, 136.71, 136.51, 135.36, 134.36, 134.30, 134.22, 134.12, 133.97, 133.67, 132.90, 130.91, 130.79, 130.35, 130.10, 129.91, 129.58, 129.08, 128.83, 127.68, 127.04, 126.80, 126.44, 123.48, 123.02, 122.81, 122.50, 121.05, 120.97, 118.35, 118.29, 118.07, 111.82, 111.60, 110.22, 108.29, 103.30, 83.58, 68.18, 45.99, 45.85, 39.07, 39.03, 38.76, 33.79, 30.28, 30.19, 29.73, 28.37, 28.28, 23.60, 23.55, 23.09, 14.06, and 10.49. ESI-HRMS (m/z): calcd for $[\text{C}_{72}\text{H}_{65}\text{N}_6\text{O}_2\text{Se}_2\text{Ir}]^+$, 1397.3225; found, 1397.3193. Anal. Calcd (%) for $\text{C}_{72}\text{H}_{65}\text{N}_6\text{O}_2\text{Se}_2\text{Ir} \cdot \text{H}_2\text{O}$: C, 61.14; H, 4.77; and N, 5.94. Found: C, 61.09; H, 4.57; and N, 6.11.

Ir-3. A purplish-red solid was obtained (80 mg, 15%). ^1H NMR (400 MHz, CDCl_3): δ (ppm) 8.87 (d, $J = 4.0$ Hz, 2H), 8.40 (d, $J = 4.0$ Hz, 2H), 8.26 (d, $J = 4.0$ Hz, 2H), 8.21 (d, $J = 8.0$ Hz, 2H), 8.06 (t, $J = 8.0$ Hz, 4H), 7.90 (d, $J = 8.0$ Hz, 2H), 7.81–7.75 (dd, $J = 8.0$, 12.0 Hz, 4H), 7.56–7.52 (m, 4H), 7.41–7.27 (m, 10H), 7.24–7.12 (m, 8H), 7.12–7.07 (m, 4H), 7.05 (d, $J = 4.0$ Hz, 2H), 6.66 (d, $J = 8.0$ Hz, 2H), 6.36 (d, $J = 8.0$ Hz, 2H), 3.98–3.95 (m, 4H), 3.26 (s, 6H), 1.88–1.83 (m, 2H), 1.36–1.28 (m, 16H), and 0.92–0.83 (m, 12H). ^{13}C NMR (400 MHz, CDCl_3): δ (ppm) 189.68, 169.11, 168.71, 161.57, 159.91, 158.79, 155.43, 151.89, 150.49, 148.85, 142.11, 141.51, 140.67, 140.56, 139.46, 136.71, 135.85, 135.68, 135.55, 134.31, 134.21, 133.67, 132.91, 132.21, 130.34, 130.11, 129.91, 129.67, 129.56, 129.07, 128.22, 127.80, 127.67, 127.57, 127.05, 126.79, 126.48, 125.36, 124.38, 123.47, 123.37, 123.00, 122.79, 122.59, 122.49, 121.86, 121.04, 120.97, 118.26, 118.06, 118.05, 111.77, 111.61, 110.21, 108.48, 100.60, 81.22, 46.06, 39.03, 33.79, 31.95, 30.07, 29.72, 29.39, 28.25, 23.48, 23.06, 22.71, 14.14, 14.07, and 10.47. ESI-HRMS (m/z): calcd for $[\text{C}_{114}\text{H}_{90}\text{N}_{10}\text{O}_2\text{S}_2\text{Ir}_2]^+$, 2080.5964; found, 2080.5947. Anal. Calcd (%) for $\text{C}_{114}\text{H}_{90}\text{Ir}_2\text{N}_{10}\text{O}_2\text{S}_2 \cdot 2\text{C}_6\text{H}_{14} \cdot 2\text{H}_2\text{O} \cdot \text{C}_3\text{H}_6\text{O}$: C, 66.02; H, 5.50; and N, 5.97. Found: C, 66.12; H, 5.45; and N, 5.60.

Ir-4. A purplish-red solid was obtained (73 mg, 14%). ^1H NMR (400 MHz, CDCl_3): δ (ppm) 8.81 (d, $J = 4.0$ Hz, 2H), 8.40 (d, $J = 8.0$ Hz, 2H), 8.26 (d, $J = 4.0$ Hz, 2H), 8.21 (d, $J = 8.0$ Hz, 2H), 8.05 (t, $J = 8.0$ Hz, 4H), 7.90 (d, $J = 8.0$ Hz, 2H), 7.81–7.75 (dd, $J = 8.0$, 12.0 Hz, 4H), 7.56–7.52 (m, 4H), 7.41–7.28 (m, 10H), 7.23–7.12 (m, 8H), 7.08–7.04 (m, 4H), 7.04 (d, $J = 4.0$ Hz, 2H), 6.67 (d, $J = 4.0$ Hz, 2H), 6.36 (d, $J = 8.0$ Hz, 2H), 3.92–3.89 (m, 4H), 3.26 (s, 6H), 1.89–1.84 (m, 2H), 1.35–1.26 (m, 16H), and 0.88–0.83 (m, 12H). ^{13}C NMR (400 MHz, CDCl_3): δ (ppm) 189.68, 159.91, 158.80, 151.92, 150.48, 141.99, 141.98, 141.50, 141.22, 140.67, 140.07, 140.01, 137.04, 136.72, 135.74, 135.54, 135.19, 134.36, 134.31, 134.22, 133.68, 132.92, 130.25, 130.14, 129.91, 129.58, 129.07, 127.68, 127.06, 126.79, 123.47, 123.01, 122.80, 122.58, 122.56, 122.50, 121.04, 120.99, 118.29, 118.07, 111.80, 111.63, 110.22, 83.64, 62.12, 46.02, 39.07, 33.79, 31.95, 31.46, 30.17, 29.73, 29.15, 28.76, 27.22, 24.86, 23.53, 23.09, 22.72, 14.05, and 10.47. ESI-HRMS (m/z): calcd for $[\text{C}_{114}\text{H}_{90}\text{N}_{10}\text{O}_2\text{Se}_2\text{Ir}_2 + \text{H}]^+$, 2175.4944; found, 2175.4924. Anal. Calcd (%) for $\text{C}_{114}\text{H}_{90}\text{Ir}_2\text{N}_{10}\text{O}_2\text{Se}_2 \cdot \text{C}_6\text{H}_{14}$: C, 63.76; H, 4.64; and N, 6.20. Found: C, 63.65; H, 4.60; and N, 6.10.

Photophysical Studies. The solvents used for photophysical studies were of spectrophotometric grade and purchased from Alfa Aesar or VWR International and used as received without further purification. The ultraviolet–visible (UV–vis) absorption spectra of ligands **3a–3d** and **4a–4d** and complexes **Ir-1–Ir-4** were recorded using a Varian Cary 50 spectrophotometer. The steady-state emission spectra in different solvents (CH₃CN, THF, CH₂Cl₂, and toluene) were recorded using a HORIBA Jobin Yvon FluoroMax-4 fluorometer/phosphorometer. The relative actinometry method was used for determining the emission quantum yields of **3a–3d**, **4a–4d**, and **Ir-1–Ir-4** with ZnTPP in toluene being used as the reference ($\lambda_{\text{max}} = 550 \text{ nm}$, $\Phi_{\text{em}} = 0.033$).⁶¹ For emission lifetime measurements, modulated pulsed excitation was delivered with a fiber-coupled pulsed UV laser (Advanced Laser Diode Systems, PiL037, 375 nm, 30 ps pulse width, 140 mW peak power, and 1 kHz modulation) fiber coupled to a photomultiplier tube (Hamamatsu H10721-20). The background-corrected intensity was collected over a broad range of emissions above 500 nm to yield spectrally integrated intensity as a function of time, which was then fit to a stretched-exponential decay $I(t) = A \exp[-(t/\tau)^\alpha]$ to extract lifetime. Slight deviations from $\alpha = 1$ reflect the width of the emission spectrum. The nanosecond transient absorption (TA) spectra and triplet lifetimes were recorded using a laser flash photolysis spectrometer (Edinburgh LP920). The excitation source was the third-harmonic output (355 nm) of a Qantel Brilliant Nd:YAG laser (pulse duration: 4.1 ns; repetition rate: 1 Hz). Each sample was purged with nitrogen for 45 min prior to the measurement.

Singlet Oxygen Measurement. Singlet oxygen generation was detected by electron paramagnetic resonance (EPR) spectroscopy in toluene using 2,2,6,6-tetramethylpiperidine (TEMP) as the singlet oxygen spin trapper. TEMP was mixed with $\sim 20\text{--}25 \mu\text{L}$ of each sample solution to reach a final sample concentration of 1 mM and TEMP concentration of 10 mM. The mixed sample was transferred into a borosilicate capillary tube (0.70 mm i.d./1.00 mm o.d.; Wilmad LabGlass, Inc.) and irradiated with a white light ($\sim 370 \text{ mW}\cdot\text{cm}^{-2}$, ACE Glass Inc. Cat.#7825-34) for a varied period of time, followed by EPR signal acquisition on a Varian E-109 spectrometer equipped with a cavity resonator for 10–30 min. All continuous wave (CW) EPR spectra were recorded with an observe power of 200 mW, a modulation frequency of 100 kHz, and a modulation amplitude of 0.5 G and scanned for 100 G from 3300 to 3400 G. The obtained CW EPR spectra are in the first derivative format.

Computational Method. All calculations were performed using the Gaussian 16 software package.⁶² The geometries of all compounds were optimized at the level of the density functional theory (DFT) using the hybrid PBE0 functional⁶³ and the mixed basis sets with LANL2DZ^{64,65} for iridium, sulfur, and selenium and 6-31G*⁶⁶ for hydrogen, carbon, nitrogen, and oxygen atoms. All calculations utilized the conductor polarized continuum model^{67,68} to implicitly introduce the toluene solvent. The UV–vis absorption spectra and fluorescence energies were computationally investigated applying linear-response time-dependent DFT (TDDFT) using the same methodology (the functional, the basis set, and the solvent model) as for the ground-state calculations. For simulations of UV–vis absorption spectra, 225 singlet optical transitions were computed by TDDFT and broadened by the empirical Gaussian function using a linewidth of 0.07 eV to reproduce the thermal broadening of spectra observed in experiments (see Figures S5–S8 in the Supporting Information). Overall, this approach has shown good agreement with experimental spectra for many heteroleptic Ir(III) complexes.^{14,47,48}

However, vibrational fine structures that are clearly seen in the experimental absorption spectra for the lowest-energy bands of **Ir-1–Ir-4** give an indication of the high degree of Frank Condon (FC) factors—the overlap between the vibrational states of two electronic states.⁶⁹ Thus, the vibronic features associated with FC overlaps cannot be neglected for the considered complexes in order to reproduce an accurate shape of their first absorption band. Therefore, FC progression^{70,71} for the first optical transition was computed for each complex to generate a vibrationally resolved electronic spectrum in the energy range of 500–800 nm. The rest of the spectrum (<500

nm) was created based on the TDDFT results without the inclusion of FC correction. The fluorescence energies were computed using the analytical gradient TDDFT^{72,73} by optimizing the lowest singlet excited state S_1 . The natures of interested optical transitions were characterized by natural transition orbitals (NTOs),⁷⁴ as implemented in Gaussian 16, which were further visualized via VMD⁷⁵ using an isovalue of 0.02.

RESULTS AND DISCUSSION

Electronic Absorption. The experimental UV–vis absorption spectra of **Ir-1–Ir-4** in toluene are displayed in Figure 1c. For comparison purposes, the absorption spectra of their

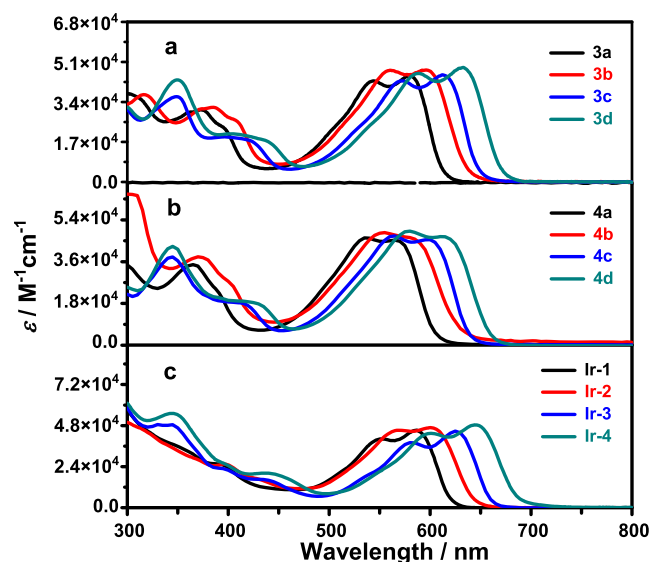


Figure 1. Experimental UV–vis absorption spectra of (a) **3a–3d**, (b) **4a–4d**, and (c) **Ir-1–Ir-4** in toluene.

corresponding ligands **3a–3d** and **4a–4d** in toluene are presented in Figure 1a,b, respectively. The absorption band maxima and molar extinction coefficients for these ligands and complexes are compiled in Table 1. Concentration-dependent studies in the range of 5×10^{-6} to $5 \times 10^{-5} \text{ mol L}^{-1}$ for **3a–3d** and **4a–4d** and 5×10^{-6} to $1 \times 10^{-4} \text{ mol L}^{-1}$ for **Ir-1–Ir-3** (Figure S4) followed Beer's law within the experimental errors, implying the absence of ground-state aggregation in the tested concentration range in toluene. However, when the concentration was higher than $1 \times 10^{-5} \text{ mol L}^{-1}$ for **Ir-4**, a shoulder appeared at ca. 700 nm, suggesting the occurrence of aggregation at higher concentrations owing to the reduced solubility of this complex in toluene. The TDDFT-calculated spectra for **3a–3d**, **4a–4d**, and **Ir-1–Ir-4** in toluene are provided in Supporting Information, Figures S5–S8, which matched the experimental spectra well with respect to the spectral features, trends, and energies. NTOs for the electrons and holes corresponding to the major transitions were generated for better understanding the nature of the electronic transitions, and the NTOs are shown in Table 2 and Supporting Information, Tables S1–S4.

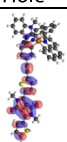
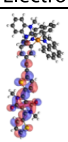
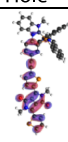
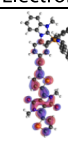
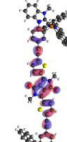

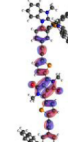
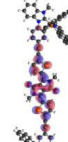
The UV–vis absorption spectra of **3a–3d** (Figure 1a) and **4a–4d** (Figure 1b) are similar in shape and energy, all possessing two major absorption bands at 300–450 nm (band I) and 450–700 nm (band II). The low-energy bands were well-resolved and exhibited large molar extinction coefficients, suggesting a $^1\pi,\pi^*$ transition in nature. Referring to the NTOs corresponding to the S_1 transitions in these compounds

Table 1. Photophysical Data for 3a–3d, 4a–4d, and Ir-1–Ir-4 in Toluene

| | $\lambda_{\text{abs}}/\text{nm}$ ($\epsilon/10^4 \text{ L}\cdot\text{mol}^{-1}\cdot\text{cm}^{-1}$) ^a | λ_f/nm (τ_f/ns), Φ_f ^b | $\lambda_{\text{T1-Tn}}/\text{nm}$ ($\tau_T/\mu\text{s}$) ^c |
|------|--------------------------------------------------------------------------------------------------------------------|---------------------------------------------------------------------|------------------------------------------------------------------------------------------|
| 3a | 374 (3.10), 544 (4.32), 580 (4.52) | 606 (4.35), 0.50 | 500 (7.30), 564 (6.72), 618 (6.03) |
| 3b | 317 (3.74), 386 (3.22), 561 (4.79), 596 (4.79) | 630 (3.20), 0.17 | 516 (0.42 (10%), 4.62 (90%)), 654 (0.41 (11%), 3.66 (89%)) |
| 3c | 348 (3.68), 573 (4.35), 612 (4.60) | 642 (3.20), 0.43 | 537 (10.55), 553 (11.79), 657 (9.23) |
| 3d | 349 (4.37), 588 (4.64), 632 (4.89) | 664 (2.70), 0.15 | 500 (9.05), 555 (10.15), 675 (0.21 (24%), 9.54 (76%)) |
| 4a | 366 (3.51), 536 (4.70), 565 (4.51) | 604 (3.82), 0.50 | 430 (5.02), 570 (4.25), 650 (3.94) |
| 4b | 373 (3.84), 555 (4.89), 581 (4.64) | 626 (2.16), 0.20 | 510 (0.15 (13%), 3.58 (87%)), 590 (0.09 (13%), 2.49 (87%)), 657 (0.12 (24%), 2.68 (76%)) |
| 4c | 344 (3.84), 564 (4.76), 599 (4.59) | 632 (2.40), 0.30 | 453 (14.0), 507 (13.7), 756 (191.0) |
| 4d | 345 (4.32), 579 (4.96), 612 (4.73) | 655 (1.74), 0.15 | 462 (13.2), 513 (13.9), 771 (124.0) |
| Ir-1 | 395 (2.56), 552 (4.08), 585 (4.56) | 613 (3.03), 0.41 | 426 (5.11), 486 (4.94), 639 (4.57), 678 (4.52), 747 (4.63) |
| Ir-2 | 397 (2.58), 570 (4.57), 601 (4.73) | 639 (3.00), 0.17 | 440 (0.51), 494 (0.57), 700 (0.54) |
| Ir-3 | 343 (4.91), 395 (2.27), 439 (1.63), 582 (3.85), 624 (4.52) | 651 (2.58), 0.34 | 462 (1.57), 666 (1.50) |
| Ir-4 | 344 (5.56), 440 (2.04), 600 (4.38), 645 (4.89) | 674 (1.66), 0.14 | 492 (0.32), 693 (0.29) |

^aAbsorption band maxima (λ_{abs}) and molar extinction coefficients (ϵ) at rt. ^bFluorescence band maxima (λ_f), lifetimes (τ_f), and quantum yields (Φ_f) for 3a–3d, 4a–4d, and Ir-1–Ir-4 at rt ($\lambda_{\text{ex}} = 550 \text{ nm}$). The reference used for the quantum yield measurement was a toluene solution of ZnTPP ($\Phi_{\text{em}} = 0.033$, $\lambda_{\text{ex}} = 550 \text{ nm}$). ^cNanosecond TA band maxima ($\lambda_{\text{T1-Tn}}$) and triplet excited-state lifetimes (τ_T).

Table 2. NTOs Representing the Lowest-Energy Singlet Transitions (S_1) for Ir-1–Ir-4 in Toluene Calculated by TDDFT Using the PBE0 Functional

| | Hole | Electron | | Hole | Electron |
|-----------------------------|-------------------------------------------------------------------------------------|-------------------------------------------------------------------------------------|-----------------------------|--------------------------------------------------------------------------------------|---------------------------------------------------------------------------------------|
| Ir-1 606 nm f = 1.563 |  |  | Ir-2 618 nm f = 1.581 |  |  |
| Ir-3 674 nm f = 2.461 |  |  | Ir-4 688 nm f = 2.476 |  |  |

(Tables S1 and S2), these absorption bands originated from the chalcogenophene–DPP $^1\pi,\pi^*$ transitions. The $^1\pi,\pi^*$ nature of the lowest-energy absorption bands in 3a–3d and 4a–4d is further supported by the minor solvatochromic effects, as shown in Supporting Information, Figure S9. For the high-energy absorption bands at <450 nm, they mainly emanated from the intramolecular charge transfer (^1ICT)/ $^1\pi,\pi^*$ (localized on chalcogenophene–DPP) transitions according to the NTOs presented in Tables S1 and S2. Compared to their respective chalcogenophene–DPP precursors,⁴² attaching 1-phenyl-NHC unit(s) in ligands 3a–3d led to a red shift of approximately 50 nm. Methylation of 3a–3d caused slight blue shifts in 4a–4d. Nonetheless, a general trend was revealed from both series of compounds. The selenophene-substituted compounds displayed a 13–20 nm red shift compared to those of the thiophene-substituted compounds, that is, 3b versus 3a, 3d versus 3c, 4b versus 4a, and 4d versus 4c. This trend is in accordance with that reported for other selenophene–DPP derivatives with respect to the thiophene–DPP derivatives.³⁵

The red-shifted absorption of the selenophene-containing compounds is ascribed to the reduced overlap of the Se orbitals with the π -orbitals of the carbon skeleton due to the larger size of the Se atom, which increases the quinoidal contribution and results in a shorter C=C double bond and larger electron delocalization.^{49–51} The compounds bearing two 1-phenyl-NHC motifs exhibited a 30–36 nm bathochromic shift due to the extended π -conjugation in comparison to those of their corresponding monosubstituted counterparts, that is, 3c versus 3a, 3d versus 3b, 4c versus 4a, and 4d versus 4b.

The absorption spectra of complexes Ir-1–Ir-4 resembled those of their corresponding ligands 4a–4d but with obvious red shifts. Similar to those of 3a–3d and 4a–4d, the vibronically resolved low-energy absorption bands at 480–700 nm can be attributed to the $^1\pi,\pi^*$ transition delocalized to the phenylethynyl chalcogenophene–DPP motifs (see NTOs for the S_1 states of these complexes in Table 2). This delocalization should be a result of the increased co-planarity due to Ir(III) complexation, which promoted the interaction

between the chalcogenophene–DPP and the ethynylphenyl components, expanded the π -conjugation, and induced the red shift of this band with respect to those in **3a–3d** and **4a–4d**. The minor solvatochromic effect manifested in Figure S9 confirmed the predominant $^1\pi,\pi^*$ transition assignment. For the absorption bands at 380–480 nm, the NTOs in Table S3 suggest mixed metal-to-ligand charge transfer ($^1\text{MLCT}$), ligand-to-ligand charge transfer ($^1\text{LLCT}$), and $^1\pi,\pi^*$ and intraligand charge transfer ($^1\text{ILCT}$) transitions. For the high-energy absorption bands at <380 nm, the dominant contributors are the $^1\pi,\pi^*$ transitions based on the cyclo-metallating C $^{\wedge}$ N ligands, mixed with $^1\text{MLCT}/^1\text{LLCT}$ and DPP-based $^1\pi,\pi^*/^1\text{ILCT}$ transitions (see NTOs in Table S4). Similar to the trend observed in **3a–3d** and **4a–4d**, replacing thiophenes with selenophenes caused the red shifts of the low-energy absorption bands in **Ir-2** and **Ir-4** relative to those in **Ir-1** and **Ir-3**, respectively. The dinuclear complexes **Ir-3** and **Ir-4** also displayed ca. 40 nm red shifts in their low-energy absorption bands with respect to those of their mononuclear counterparts **Ir-1** and **Ir-2**, respectively.

Photoluminescence. The emission of **3a–3d**, **4a–4d**, and **Ir-1–Ir-4** was studied in different solvents at rt. The emission spectra in toluene are displayed in Figure 2, and the emission

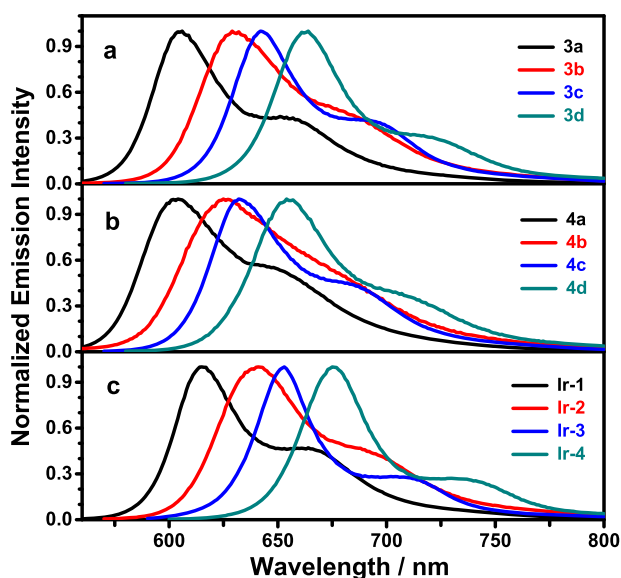


Figure 2. Normalized experimental emission spectra of (a) **3a–3d**, (b) **4a–4d**, and (c) **Ir-1–Ir-4** at rt in toluene. $c = 1 \times 10^{-5}$ mol L $^{-1}$.

band maxima (λ_f), lifetime (τ_f), and quantum yield (Φ_f) are listed in Table 1. The normalized emission spectra and emission data in other solvents are provided in Figure S10 and Table S5 in the Supporting Information.

The emission spectra of all compounds are mirror images to their corresponding excitation spectra, with Stokes shifts in the range of 689–1237 cm $^{-1}$. The emission lifetimes are in the range of 1.66–4.35 ns, and the emission intensity is insensitive to oxygen. All these emission characters are indicative of fluorescence in nature. The vibronic structures, minor solvatochromic effects (Figure S10 and Table S5), and the TDDFT calculation results for **Ir-1–Ir-4** in toluene (Table S6) suggest that the emitting states are primarily the chalcogenophene–DPP-localized $^1\pi,\pi^*$ S_1 states. The fluorescence spectra of **3a–3d**, **4a–4d**, and **Ir-1–Ir-4** all resembled each other, and the trends of the fluorescence energies followed the same

trends as those observed from their absorption spectra, that is, (i) the fluorescence spectra of **4a–4d** were somewhat blue-shifted compared to those of **3a–3d**, while the spectra of the complexes **Ir-1–Ir-4** were red-shifted compared to those of **3a–3d** and **4a–4d** owing to the increased co-planarity and extended π -conjugation in the complexes; (ii) within each series of compounds, selenophene substitution caused red-shifted fluorescence compared to thiophene substitution due to the larger size of Se and the increased quinoid structure, and incorporation of 1-phenyl-NHC or its Ir(III) complex to both sides of chalcogenophene–DPP induced further red shifts in the emission with respect to the one-side substituted counterparts.

Structural variations not only impacted the fluorescence energies but also influenced τ_f and Φ_f in a systematic way. As displayed in Table 1, the τ_f in toluene decreased in selenophene-containing compounds with respect to their corresponding thiophene-containing compounds; di(1-phenyl-NHC) substitution shortened the τ_f compared to mono(1-phenyl-NHC) substitution. In addition, the τ_f values of **3a–3d** were generally longer than those of their corresponding compounds in **4a–4d** and their Ir(III) complexes. These trends should be mainly attributed to the heavy-atom effect from Se, I $^-$, and/or Ir(III), which increased the ISC to the triplet excited state (T_1) and thus depopulated the S_1 state. The Φ_f values of the corresponding compounds between **3a–3d** and **4a–4d** were quite similar, but the Φ_f values in their respective Ir(III) complexes were significantly lower due to the heavy-atom-induced rapid ISC to the T_1 state (Figure 3),

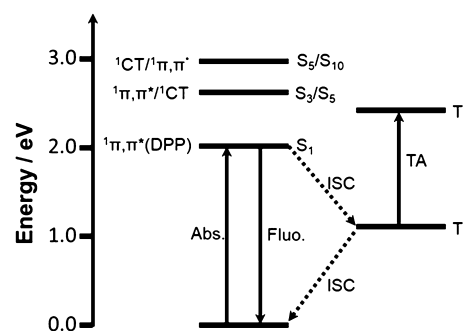


Figure 3. Simplified Jablonski diagram for compounds **Ir-1–Ir-4** in toluene. The energies of the singlet excited states are estimated based on the TDDFT calculation results. The T_1 energy is estimated from the phosphorescence energy reported for the cationic dinuclear Ir(III) complex tethered by DPP.⁴¹ States S_3/S_5 indicate the third singlet excited state in **Ir-1** and **Ir-2** and the fifth singlet excited state in **Ir-3** and **Ir-4** and S_5/S_{10} refer to the fifth and 10th singlet excited states in **Ir-1/Ir-2** and **Ir-3/Ir-4**, respectively. ISC refers to intersystem crossing, and TA indicates the transient absorption.

which consequently decreased the fluorescence intensity and lifetime. For the same reason, the Φ_f values were pronouncedly decreased in the selenophene-containing compounds compared to those of the thiophene-containing ones.⁷⁶ In contrast, although the di(1-phenyl-NHC) substitution attenuated the fluorescence efficiencies in **3c/4c** and **3d/4d** with respect to those of their mono(1-phenyl-NHC)-substituted analogues **3a/4a** and **3b/4b**, respectively, owing to the reduced fluorescence energies in the disubstituted compounds (which increased the nonradiative decay rates according to the energy gap law⁷⁷), the quantum yield reduction became much less pronounced, especially in the selenophene-containing com-

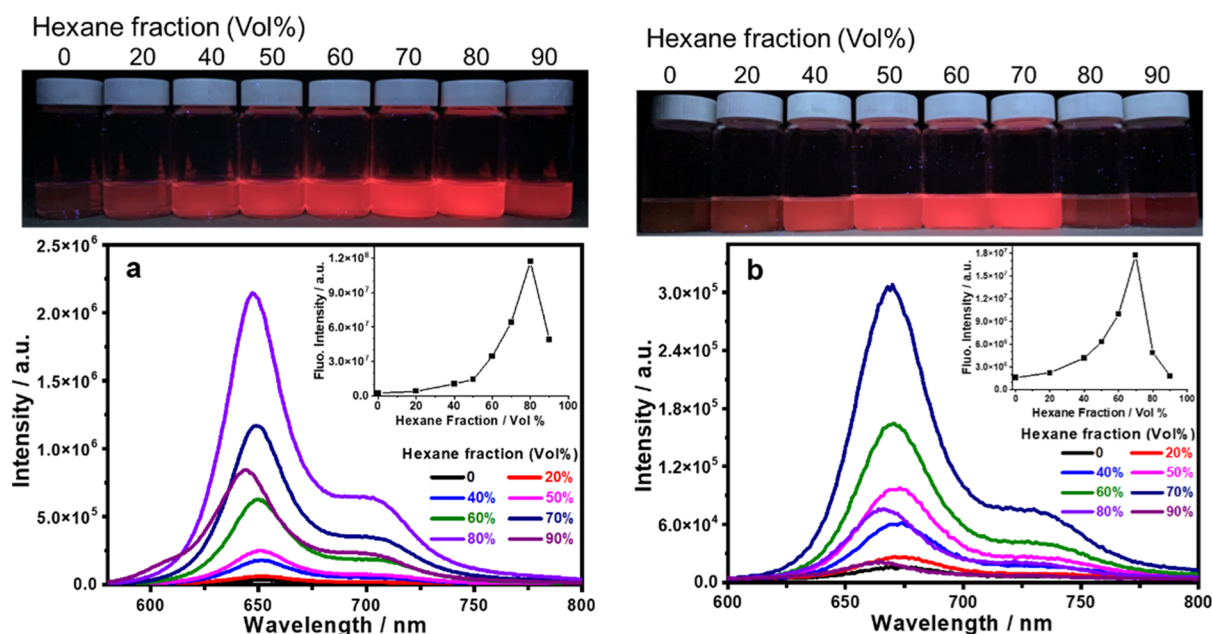


Figure 4. Emission spectra and photographs of (a) Ir-3 and (b) Ir-4 in the CH_2Cl_2 /hexane mixture with different hexane fractions at rt. $c = 1 \times 10^{-5} \text{ mol L}^{-1}$. The inset shows the fluorescence intensity (i.e., the integrated area underneath the spectrum) versus hexane fraction.

pounds **3d/4d** compared to those of **3b/4b**. This phenomenon implies that the heavy-atom effect plays the major role in decreasing Φ_f .

It should be noted that although the polarity of the solvent exhibited a minor effect on the emission energy of each compound, the effect of different solvents on Φ_f was substantial. Analysis of the Φ_f data in Table S5 revealed a general trend, that is, the polar solvent decreased the Φ_f values significantly, indicating the increased ratio of the nonradiative decay rate (k_{nr}) versus the radiative decay rate (k_r) in polar solvents. For Ir-1–Ir-4, the very low emission quantum yields are ascribed to their poor solubility in polar solvents. Although the dilute solutions ($\sim 2 \times 10^{-6} \text{ mol L}^{-1}$) in polar solvents appeared to be transparent after sonication, the complexes could still present as oligomers in these solutions. This notion can be supported by the following facts: (1) the vibronic structure of the low-energy absorption band of Ir-4 in CH_3CN was lost and a shoulder appeared at 702 nm (Figure S9); (2) the emission of Ir-4 in CH_3CN was red-shifted to 713 nm (Figure S10); (3) all samples were trapped in the $0.2 \mu\text{m}$ syringe filter and left the blank CH_3CN solvent after the dilute CH_3CN solution used for the quantum yield measurement was filtered; and (4) aggregation also occurred for Ir-4 in toluene when concentrations were higher than $1 \times 10^{-5} \text{ mol L}^{-1}$ as a shoulder appeared at ca. 700 nm (Figure S4) even if it is the best solvent to dissolve this complex. In CH_2Cl_2 and THF solutions, although aggregation was not clearly evidenced from the UV–vis absorption and emission spectra of Ir-4 and for the other three complexes in polar solvents, it is reasonable to believe that they all present as oligomers or small-size aggregates based on the similarly low-emission quantum yields of these complexes in these polar solvents.

Emission of the complexes Ir-1–Ir-4 was further studied in a mixed solvent of CH_2Cl_2 (better solvent) and hexane (poor solvent) with varied volume compositions. As shown in Figure 4A for Ir-3, the emission intensity gradually increased when the volume fraction of hexane increased from 0 to 80%. Beyond 80% fraction, the emission intensity started to

decrease. At a first glimpse, this phenomenon resembles the aggregation-induced emission (AIE).⁷⁸ However, considering the drastically higher emission quantum yields of these complexes in less polar solvents such as toluene, the enhanced emission upon the addition of hexane could be the result of reduced solvent polarity. To verify this possibility, the emission quantum yields of these complexes were measured in hexane, and the results are presented in Table S5. For Ir-1 and Ir-2, their Φ_f values in hexane are 61- and 38-fold of those in CH_2Cl_2 , respectively. The Φ_f values of Ir-3 and Ir-4 in hexane were unable to be determined because of their very poor solubility in hexane. When the hexane concentration reached 80%, the formed aggregates started to precipitate out, reducing the concentration of the emissive monomers, and thus, the emission intensity decreased. Ir-1, Ir-2, and Ir-4 also exhibited a similar behavior in the mixed CH_2Cl_2 and hexane solutions (Figures 4b and S12) but with the highest emission intensity being reached at 70% of hexane fraction for Ir-4 and at 95% of hexane fraction for Ir-1 and Ir-2. This difference should be ascribed to the poorer solubility of Ir-4 but better solubility of Ir-1 and Ir-2 compared to that of Ir-3 in both CH_2Cl_2 and hexane.

The dynamic light scattering measurement of Ir-3 and Ir-4 in mixed CH_2Cl_2 /hexane solutions with 95% of hexane fraction (v/v) revealed number-averaged hydrodynamic diameters of approximately 18 and 13 nm at the concentrations of 2.5×10^{-6} and $1.65 \times 10^{-6} \text{ mol L}^{-1}$, respectively (Figure S13). For Ir-3, a number-averaged hydrodynamic diameter of approximately 14 nm was also detected in a $5.0 \times 10^{-6} \text{ mol L}^{-1}$ CH_2Cl_2 /hexane solution with 90% of hexane fraction (v/v). However, the size of aggregates was too small to be detected when the hexane fraction was lower than 90% for Ir-3 and <95% for Ir-4 due to the instrument resolution (0.2 nm).

To further exclude the presence of AIE, the absorption and emission of Ir-1 in the mixed CH_3CN and H_2O medium were studied. This solvent system was chosen because of the similar polarity of CH_3CN and H_2O , which minimizes the impact of

solvent polarity change on the emission intensity. In addition, Ir-1 has the best solubility in CH₃CN among the four Ir(III) complexes. As shown in Figure S14, with the increased H₂O fraction, the low-energy absorption band became broader and significantly red-shifted with an increased baseline; meanwhile, the fluorescence intensity kept decreasing. These phenomena indicate the formation of aggregates in the mixed CH₃CN/H₂O solutions, and aggregation quenches the emission. This experiment provides additional support that the enhanced emission in CH₂Cl₂/hexane is due to the reduced polarity of the solvent media when the hexane fraction increased. It also approves that the aggregation quenched the emission in these complexes.

Transient Absorption. It was reported that the phosphorescence of the thiophene–DPP bridged cationic dinuclear Ir(III) complex appeared at >900 nm at 77 K.⁴¹ However, the phosphorescence of 3a–3d, 4a–4d, and Ir-1–Ir-4 was too weak to be monitored at rt, which prevented us from studying the triplet excited-state characteristics via phosphorescence. Nevertheless, the triplet excited-state lifetime can be investigated via the time-resolved TA spectroscopy. The nanosecond TA of 3a–3d, 4a–4d, and Ir-1–Ir-4 was investigated in deaerated toluene. The obtained TA spectra at zero delay after 355 nm excitation are illustrated in Figure 5,

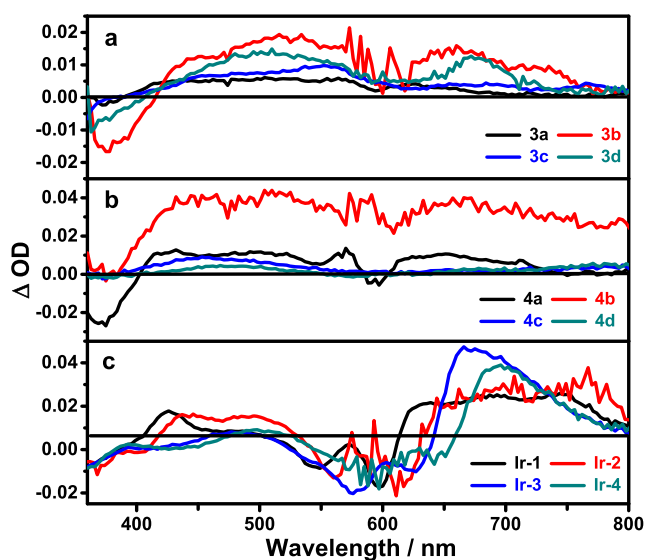


Figure 5. Nanosecond TA spectra of (a) 3a–3d, (b) 4a–4d, and (c) Ir-1–Ir-4 in a deaerated toluene solution at zero delay after 355 nm excitation ($A_{355} = 0.4$ in a 1 cm cuvette). 4c and 4d were measured in mixed toluene/methanol (50:50, v/v) due to their poor solubility in toluene.

and the TA band maxima and the triplet excited-state lifetimes deduced from the decay of the TA signals at various TA band maxima are listed in Table 1. The time-resolved TA spectra of these compounds and the kinetic decay curves at the respective TA band maximum for each compound are provided in Supporting Information, Figures S15 and S16.

The TA spectra of 3a–3d possessed broad positive absorption bands at 410–750 nm (for 3c, the positive band extended to 800 nm). Three general trends were observed based on the spectral features and the T_1 lifetimes: (i) the TA intensity of the selenophene-containing compound 3b is much larger than that of the thiophene-containing compound 3a, while the T_1 lifetime of 3b is shorter than that of 3a. This

phenomenon can be rationalized by the heavy-atom (Se)-enhanced ISC, which facilitates the population of the triplet excited state in 3b and consequently increased the quantum yield of the triplet excited-state formation and enhanced the triplet excited-state absorption. Meanwhile, the rapid ISC also facilitates the decay of T_1 to S_0 , shortening the T_1 lifetime of 3b compared to that of 3a. (ii) The T_1 lifetimes of 3c and 3d are much longer than those of 3a and 3b, respectively, due to the extended π -conjugation in 3c and 3d compared to that in 3a and 3b. The expansive π -conjugation probably reduces the contribution of the d orbitals in S and Se to the frontier molecular orbitals of 3c and 3d, undermining the heavy-atom effects of Se in 3d. As a result, the impacts of the selenophene versus thiophene substitution on the TA intensities and lifetimes of 3d versus 3c become much less pronounced.

For compounds 4a and 4b, their TA spectral features resembled those of 3a and 3b, respectively, but with a much enhanced TA intensity. Meanwhile, the T_1 lifetimes were obviously shorter than their counterparts 3a and 3b. These changes could likely be attributed to the additional heavy-atom effect induced by I[−]. In 4c and 4d, the shape of the TA spectra resembled each other, but the maximum of the 400–570 nm band was red-shifted in 4d. However, their T_1 lifetimes resembled each other.

The TA spectral features of Ir-1–Ir-4 resembled those of the reported cationic Ir(III) complexes bearing the DPP unit,^{42,43} while their TA intensities were much stronger than their corresponding compounds 3a–3d and 4a–4d, especially the absorption in the red to NIR regions was prominent. The T_1 lifetimes of Ir-2–Ir-4 were significantly shorter than those of 3b–3d and 4b–4d. The shapes of the TA spectra of Ir-1 and Ir-2 were alike each other and those of Ir-3 and Ir-4 were in resemblance to each other. However, the absorption band maxima of the selenophene-containing complexes, that is, Ir-2 and Ir-4, were red-shifted compared to those of their thiophene-containing counterparts Ir-1 and Ir-3, respectively, and the T_1 lifetimes of Ir-2 and Ir-4 were markedly shorter than those of Ir-1 and Ir-3. In addition, complexation with two Ir(III) ions in Ir-3 and Ir-4 shortened their T_1 lifetimes with respect to those of their mononuclear counterparts Ir-1 and Ir-2, accompanied by somewhat enhanced TA signals in the red–NIR regions. All these observations are in accordance with the promoted ISC by the heavy Ir(III) ion. A general conclusion that can be drawn is that complexation with the heavy Ir(III) ion facilitated the population of the triplet excited states in these complexes, which enhanced the TA signals; on the other hand, it also aided the decay from the T_1 to S_0 state and thus shortened the T_1 lifetimes.

Singlet Oxygen Measurement. Both the photoluminescence and TA studies suggest that Ir(III) complexation enhanced the T_1 state formation, together with the moderate to long T_1 lifetimes, Ir-1–Ir-4 could potentially generate singlet oxygen via energy transfer in aerated solutions. To verify this possibility, EPR spectroscopy was used to detect the singlet oxygen generation by utilizing TEMP as the spin trapper. Figure 6 shows the irradiation time-dependent EPR signals for Ir-1. The EPR signals for Ir-2–Ir-4 are provided in Supporting Information, Figure S17. The three-line signals represent the typical EPR signals for the TEMP-¹O₂ adduct, that is, TEMPO, testifying the ¹O₂ generation upon white light irradiation. As expected, the production of ¹O₂ followed a time-dependent fashion. The TEMPO signals increased with prolonged irradiation time until reaching a maximum point.

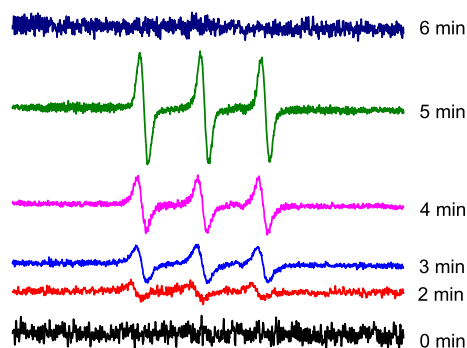


Figure 6. Time-dependent EPR signals of Ir-1 (1 mM + 10 mM TEMP) in toluene.

After that, the signal intensity decreased, presumably due to the consumption of oxygen in the sample solution.

CONCLUSIONS

We have synthesized four neutral Ir(III) complexes Ir-1–Ir-4 bearing a DPP-substituted NHC ligand. Spectroscopic studies and DFT calculations on these complexes and their corresponding ligands suggest that the singlet excited-state properties including the UV–vis absorption and fluorescence are dominated by the properties of their respective ligands. Replacing the thiophene substituents by selenophene substituents on DPP caused pronounced red shifts in both the absorption and emission spectra, and incorporation of two (NHC)Ir(bqu)₂ units further lowered the energies of the S₁ states in the bimetallic complexes compared to those of the monometallic complexes. As expected, the heavy-atom effects induced by Ir(III) led to a reduced fluorescence quantum yield and shorter fluorescence lifetime in Ir-2 and Ir-4 compared to their monometallic counterparts Ir-1 and Ir-3, respectively. On the other hand, the increased triplet excited-state population induced by the heavy Se and Ir(III) enhanced the triplet excited-state absorption of these complexes with respect to their corresponding ligands, and these complexes also manifested the ability of singlet oxygen production upon white light activation. The potential of utilizing these complexes as photosensitizers for PDT will be studied in the near future after they are encapsulated into amphiphilic polymer micelles to improve their dispersity in aqueous solution.

ASSOCIATED CONTENT

Supporting Information

The Supporting Information is available free of charge at <https://pubs.acs.org/doi/10.1021/acs.inorgchem.1c01848>.

¹H NMR, ¹³C NMR, and high-resolution mass spectra of Ir-1–Ir-4; comparison of the experimental and theoretical UV–vis absorption spectra of 3a–3d, 4a–4d, and Ir-1–Ir-4 in toluene; absorption spectra of 3a–3d, 4a–4d, and Ir-1–Ir-4 in toluene at different concentrations; comparison of the emission spectra and the calculated emission energies of Ir-1–Ir-4 in toluene; absorption spectra, emission spectra, and data of 3a–3d, 4a–4d, and Ir-1–Ir-4 in different solvents at rt; NTOs of 3a–3d, 4a–4d, and Ir-1–Ir-4 in toluene; emission of Ir-1 and Ir-2 in CH₂Cl₂/hexane; absorption and emission of Ir-1 in CH₃CN/H₂O; percentage particle number versus particle size plots; time-resolved TA spectra and kinetic

curves of 3a–3d, 4a–4d, and Ir-1–Ir-4 in toluene; time-dependent EPR signals of Ir-2–Ir-4 in toluene; and full author list for refs 15, 16, 44, and 62 (PDF)

AUTHOR INFORMATION

Corresponding Author

Wenfeng Sun – Department of Chemistry and Biochemistry, North Dakota State University, Fargo, North Dakota 58108, United States; orcid.org/0000-0003-3608-611X; Email: Wenfeng.Sun@ndsu.edu

Authors

Wan Xu – Department of Chemistry and Biochemistry, North Dakota State University, Fargo, North Dakota 58108, United States; Engineering Research Center for Nanomaterials, Henan University, Kaifeng, Zhengzhou Province 475004, P. R. China

Levi Lystrom – Department of Chemistry and Biochemistry, North Dakota State University, Fargo, North Dakota 58108, United States; orcid.org/0000-0001-6369-8643

Yanxiong Pan – Department of Chemistry and Biochemistry, North Dakota State University, Fargo, North Dakota 58108, United States

Xinyang Sun – Department of Chemistry and Biochemistry, North Dakota State University, Fargo, North Dakota 58108, United States

Salim A. Thomas – Materials and Nanotechnology Program, North Dakota State University, Fargo, North Dakota 58108, United States

Svetlana V. Kilina – Department of Chemistry and Biochemistry, North Dakota State University, Fargo, North Dakota 58108, United States; orcid.org/0000-0003-1350-2790

Zhongyu Yang – Department of Chemistry and Biochemistry, North Dakota State University, Fargo, North Dakota 58108, United States; orcid.org/0000-0002-3018-3608

Hua Wang – Engineering Research Center for Nanomaterials, Henan University, Kaifeng, Zhengzhou Province 475004, P. R. China; orcid.org/0000-0003-3239-1600

Erik K. Hobbie – Materials and Nanotechnology Program, Department of Physics, and Department of Coatings and Polymeric Materials, North Dakota State University, Fargo, North Dakota 58108, United States; orcid.org/0000-0001-6158-8977

Complete contact information is available at: <https://pubs.acs.org/doi/10.1021/acs.inorgchem.1c01848>

Notes

The authors declare no competing financial interest.

ACKNOWLEDGMENTS

W.S. and S.V.K. acknowledge the financial support from the National Science Foundation (CHE-1800476) for compound synthesis, photophysical studies, and computational simulations.

REFERENCES

- (1) Lu, H.; Mack, J.; Yang, Y.; Shen, Z. Structural Modification Strategies for the Rational Design of Red/NIR Region BODIPYs. *Chem. Soc. Rev.* **2014**, *43*, 4778–4823.
- (2) Luo, X.; Li, J.; Zhao, J.; Gu, L.; Qian, X.; Yang, Y. A General Approach to the Design of High-Performance Near-Infrared (NIR) D-π-A Type Fluorescent Dyes. *Chin. Chem. Lett.* **2019**, *30*, 839–846.

- (3) Ho, C.-L.; Li, H.; Wong, W.-Y. Red to Near-Infrared Organometallic Phosphorescent Dyes for OLED Applications. *J. Organomet. Chem.* **2014**, *751*, 261–285.
- (4) Escobedo, J. O.; Rusin, O.; Lim, S.; Strongin, R. M. NIR Dyes for Bioimaging Applications. *Curr. Opin. Chem. Biol.* **2010**, *14*, 64–70.
- (5) Luo, S.; Zhang, E.; Su, Y.; Cheng, T.; Shi, C. A Review of NIR Dyes in Cancer Targeting and Imaging. *Biomaterials* **2011**, *32*, 7127–7138.
- (6) Qian, G.; Wang, Z. Y. Near-infrared Organic Compounds and Emerging Applications. *Chem. Asian J.* **2010**, *5*, 1006–1029.
- (7) Kiyose, K.; Kojima, H.; Nagano, T. Functional Near-Infrared Fluorescent Probes. *Chem. Asian J.* **2008**, *3*, 506–515.
- (8) Bulach, V.; Sguerra, F.; Hosseini, M. W. Porphyrin Lanthanide Complexes for NIR Emission. *Coord. Chem. Rev.* **2012**, *256*, 1468–1478.
- (9) Pansare, V. J.; Hejazi, S.; Faenza, W. J.; Prud'homme, R. K. Review of Long-Wavelength Optical and NIR Imaging Materials: Contrast Agents, Fluorophores, and Multifunctional Nano Carriers. *Chem. Mater.* **2012**, *24*, 812–827.
- (10) Zhang, D.; Wu, M.; Zeng, Y.; Wu, L.; Wang, Q.; Han, X.; Liu, X.; Liu, J. Chlorin e6 Conjugated Poly(Dopamine) Nanospheres as PDT/PTT Dual-Modal Therapeutic Agents for Enhanced Cancer Therapy. *ACS Appl. Mater. Interfaces* **2015**, *7*, 8176–8187.
- (11) Atchison, J.; Kamila, S.; Nesbitt, H.; Logan, K. A.; Nicholas, D. M.; Fowley, C.; Davis, J.; Callan, B.; McHale, A. P.; Callan, J. F. Iodinated Cyanine Dyes: A New Class of Sensitisers for Use in NIR Activated Photodynamic Therapy (PDT). *Chem. Commun.* **2017**, *53*, 2009–2012.
- (12) Turksoy, A.; Yildiz, D.; Akkaya, E. U. Photosensitization and Controlled Photosensitization with BODIPY Dyes. *Coord. Chem. Rev.* **2019**, *379*, 47–64.
- (13) Huang, L.; Wu, W.; Li, Y.; Huang, K.; Zeng, L.; Lin, W.; Han, G. Highly Effective Near-Infrared Activating Triplet–Triplet Annihilation Upconversion for Photoredox Catalysis. *J. Am. Chem. Soc.* **2020**, *142*, 18460–18470.
- (14) Liu, B.; Lystrom, L.; Cameron, C. G.; Kilina, S.; McFarland, S. A.; Sun, W. Monocationic Iridium(III) Complexes with Far-Red Charge Transfer Absorption and Near-IR Emission: Synthesis, Photophysics, and Reverse Saturable Absorption. *Eur. J. Inorg. Chem.* **2019**, 2208–2215.
- (15) Roque, J. A.; Barrett, P. C.; Cole, H. D.; Lifshits, L. M.; Shi, G.; Monroe, S.; von Dahlen, D.; Kim, S.; Russo, N.; Deep, G.; et al. Breaking the Barrier: An Osmium Photosensitizer with Unprecedented Hypoxic Phototoxicity for Real World Photodynamic Therapy. *Chem. Sci.* **2020**, *11*, 9784–9806.
- (16) Lifshits, L. M.; Roque III, J. A.; Konda, P.; Monroe, S.; Cole, H. D.; von Dahlen, D.; Kim, S.; Deep, G.; Thummel, R. P.; Cameron, C. G.; et al. Near-Infrared Absorbing Ru(II) Complexes Act as Immunoprotective Photodynamic Therapy (PDT) Agents against Aggressive Melanoma. *Chem. Sci.* **2020**, *11*, 11740–11762.
- (17) Wang, L.; Yin, H.; Cui, P.; Hetu, M.; Wang, C.; Monroe, S.; Schaller, R. D.; Cameron, C. G.; Liu, B.; Kilina, S.; McFarland, S. A.; Sun, W. Near-Infrared-Emitting Heteroleptic Cationic Iridium Complexes Derived from 2,3-Diphenylbenzo[g]quinoxaline as In Vitro Theranostic PDT Agents. *Dalton Trans.* **2017**, *46*, 8091–8103.
- (18) Ramu, V.; Gautam, S.; Garai, A.; Kondaiah, P.; Chakravarty, A. R. Glucose-Appended Platinum(II)-BODIPY Conjugates for Targeted Photodynamic Therapy in Red Light. *Inorg. Chem.* **2018**, *57*, 1717–1726.
- (19) Goswami, S.; Winkel, R. W.; Alarousu, E.; Ghiviriga, I.; Mohammed, O. F.; Schanze, K. S. Photophysics of Organometallic Platinum(II) Derivatives of the Diketopyrrolopyrrole Chromophore. *J. Phys. Chem. A* **2014**, *118*, 11735–11743.
- (20) Majumdar, P.; Yuan, X.; Li, S.; Le Guennic, B.; Ma, J.; Zhang, C.; Jacquemin, D.; Zhao, J. Cyclometalated Ir(III) Complexes with Styryl-BODIPY Ligands Showing near IR Absorption/Emission: Preparation, Study of Photophysical Properties and Application as Photodynamic/Luminescence Imaging Materials. *J. Mater. Chem. B* **2014**, *2*, 2838–2854.
- (21) Yang, Q.; Jin, H.; Gao, Y.; Lin, J.; Yang, H.; Yang, S. Photostable Iridium(III)-Cyanine Complex Nanoparticles for Photoacoustic Imaging Guided Near-Infrared Photodynamic Therapy in Vivo. *ACS Appl. Mater. Interfaces* **2019**, *11*, 15417–15425.
- (22) Duffy, M. J.; Planas, O.; Faust, A.; Vogl, T.; Hermann, S.; Schäfers, M.; Nonell, S.; Strassert, C. A. Towards Optimized Naphthalocyanines as Sonochromes for Photoacoustic Imaging In Vivo. *Photoacoustics* **2018**, *9*, 49–61.
- (23) Harriman, A.; Maiya, B. G.; Murai, T.; Hemmi, G.; Sessler, J. L.; Mallouk, T. E. Metallotexaphyrins: A New Family of Photosensitisers for Efficient Generation of Singlet Oxygen. *J. Chem. Soc., Chem. Commun.* **1989**, 314–316.
- (24) Zhao, J.; Yan, K.; Xu, G.; Liu, X.; Zhao, Q.; Xu, C.; Gou, S. An Iridium (III) Complex Bearing a Donor–Acceptor–Donor Type Ligand for NIR-Triggered Dual Phototherapy. *Adv. Funct. Mater.* **2020**, *31*, 2008325.
- (25) Huang, H.; Banerjee, S.; Sadler, P. J. Recent Advances in the Design of Targeted Iridium(III) Photosensitizers for Photodynamic Therapy. *ChemBioChem* **2018**, *19*, 1574–1589.
- (26) Huang, T.; Yu, Q.; Liu, S.; Huang, W.; Zhao, Q. Phosphorescent Iridium(III) Complexes: A Versatile Tool for Biosensing and Photodynamic Therapy. *Dalton Trans.* **2018**, *47*, 7628–7633.
- (27) Qiu, K.; Chen, Y.; Rees, T. W.; Ji, L.; Chao, H. Organelle-Targeting Metal Complexes: From Molecular Design to Bio-Applications. *Coord. Chem. Rev.* **2019**, *378*, 66–86.
- (28) Chen, Y.; Guan, R.; Zhang, C.; Huang, J.; Ji, L.; Chao, H. Two-Photon Luminescent Metal Complexes for Bioimaging and Cancer Phototherapy. *Coord. Chem. Rev.* **2016**, *310*, 16–40.
- (29) Wang, L.; Cui, P.; Liu, B.; Kilina, S.; Sun, W. Novel N₆ Trisbidentate Ligand Coordinated Ir(III) Complexes and Their Ru(II) Analogs. *Dalton Trans.* **2018**, *47*, 13776–13780.
- (30) Collin, J.-P.; Dixon, I. M.; Sauvage, J.-P.; Williams, J. A. G.; Barigelli, F.; Flamigni, L. Synthesis and Photophysical Properties of Iridium(III) Bisterpyridine and Its Homologues: a Family of Complexes with a Long-Lived Excited State. *J. Am. Chem. Soc.* **1999**, *121*, 5009–5016.
- (31) Liu, B.; Monroe, S.; Li, Z.; Javed, M. A.; Ramirez, D.; Cameron, C. G.; Colón, K.; Roque, J., III; Kilina, S.; Tian, J.; McFarland, S. A.; Sun, W. A New Class of Homoleptic and Heteroleptic Bis-(terpyridine) Iridium(III) Complexes with Strong Photodynamic Therapy Effects. *ACS Appl. Bio Mater.* **2019**, *2*, 2964–2977.
- (32) Cotton, F. A.; Wilkinson, G. *Advanced Inorganic Chemistry: A Comprehensive Text*; Wiley: New York, 1980.
- (33) Qiao, Y.; Guo, Y.; Yu, C.; Zhang, F.; Xu, W.; Liu, Y.; Zhu, D. Diketopyrrolopyrrole-Containing Quinoidal Small Molecules for High-Performance, Air-Stable, and Solution-Processable n-Channel Organic Field-Effect Transistors. *J. Am. Chem. Soc.* **2012**, *134*, 4084–4087.
- (34) Yum, J.-H.; Holcombe, T. W.; Kim, Y.; Yoon, J.; Rakstys, K.; Nazeeruddin, M. K.; Grätzel, M. Towards High-Performance DPP-Based Sensitizers for DSC Applications. *Chem. Commun.* **2012**, *48*, 10727–10729.
- (35) Dhar, J.; Venkatramiah, N.; Anitha, A.; Patil, S. Photophysical Electrochemical and Solid State Properties of Diketopyrrolopyrrole Based Molecular Materials: Importance of the Donor Group. *J. Mater. Chem. C* **2014**, *2*, 3457–3466.
- (36) Chan, W. K.; Chen, Y.; Peng, Z.; Yu, L. Rational Designs of Multifunctional Polymers. *J. Am. Chem. Soc.* **1993**, *115*, 11735–11743.
- (37) Qu, Y.; Hua, J.; Tian, H. Colorimetric and Ratiometric Red Fluorescent Chemosensor for Fluoride Ion Based on Diketopyrrolopyrrole. *Org. Lett.* **2010**, *12*, 3320–3323.
- (38) Qiao, Z.; Xu, Y.; Lin, S.; Peng, J.; Cao, D. Synthesis and characterization of red-emitting diketopyrrolopyrrole-alt-phenylenevinylene polymers. *Synth. Met.* **2010**, *160*, 1544–1550.
- (39) Wienk, M. M.; Turbiez, M.; Gilot, J.; Janssen, R. A. J. Narrow-Bandgap Diketopyrrolopyrrole Polymer Solar Cells: The Effect of Processing on the Performance. *Adv. Mater.* **2008**, *20*, 2556–2560.

- (40) Holcombe, T. W.; Yum, J.-H.; Yoon, J.; Gao, P.; Marszalek, M.; Censo, D. D.; Rakstys, K.; Nazeeruddin, M. K.; Graetzel, M. A Structural Study of DPP-Based Sensitizers for DSC Applications. *Chem. Commun.* **2012**, 48, 10724–10726.
- (41) Bürckstümmer, H.; Weissenstein, A.; Bialas, D.; Würthner, F. J. Synthesis and Characterization of Optical and Redox Properties of Bithiophene-Functionalized Diketopyrrolopyrrole Chromophores. *J. Org. Chem.* **2011**, 76, 2426–2432.
- (42) McCusker, C. E.; Hablot, D.; Ziessel, R.; Castellano, F. N. Metal Coordination Induced π -Extension and Triplet State Production in Diketopyrrolopyrrole Chromophores. *Inorg. Chem.* **2012**, 51, 7957–7959.
- (43) McCusker, C. E.; Hablot, D.; Ziessel, R.; Castellano, F. N. Triplet State Formation in Homo- and Heterometallic Diketopyrrolopyrrole Chromophores. *Inorg. Chem.* **2014**, 53, 12564–12571.
- (44) Wang, L.; Monro, S.; Cui, P.; Yin, H.; Liu, B.; Cameron, C. G.; Xu, W.; Hetu, M.; Fuller, A.; Kilina, S.; et al. Heteroleptic Ir(III) N_6 Complexes with Long-Lived Triplet Excited States and In Vitro Photobiological Activities. *ACS Appl. Mater. Interfaces* **2019**, 11, 3629–3644.
- (45) Liu, B.; Monro, S.; Javed, M. A.; Cameron, C. G.; Colón, K. L.; Xu, W.; Kilina, S.; McFarland, S. A.; Sun, W. Neutral Iridium(III) Complexes Bearing BODIPY-Substituted N-Heterocyclic Carbene (NHC) Ligands: Synthesis, Photophysics, In Vitro Theranostic Photodynamic Therapy, and Antimicrobial Activity. *Photochem. Photobiol. Sci.* **2019**, 18, 2381–2396.
- (46) Lu, C.; Xu, W.; Shah, H.; Liu, B.; Xu, W.; Sun, L.; Qian, S. Y.; Sun, W. In vitro Photodynamic Therapy of Mononuclear and Dinuclear Iridium(III) Bis(terpyridine) Complexes. *ACS Appl. Bio Mater.* **2020**, 3, 6865–6875.
- (47) Liu, B.; Monro, S.; Lystrom, L.; Cameron, C. G.; Colón, K.; Yin, H.; Kilina, S.; McFarland, S. A.; Sun, W. Photophysical and Photobiological Properties of Dinuclear Iridium(III) Bis-tridentate Complexes. *Inorg. Chem.* **2018**, 57, 9859–9872.
- (48) Wang, C.; Lystrom, L.; Yin, H.; Hetu, M.; Kilina, S.; McFarland, S. A.; Sun, W. Increasing the Triplet Lifetime and Extending the Ground-State Absorption of Biscyclometalated Ir(III) Complexes for Reverse Saturable Absorption and Photodynamic Therapy Applications. *Dalton Trans.* **2016**, 45, 16366–16378.
- (49) McCormick, T. M.; Jahnke, A. A.; Lough, A. J.; Seferos, D. S. Tellurophenes with Delocalized π -Systems and Their Extended Valence Adducts. *J. Am. Chem. Soc.* **2012**, 134, 3542–3548.
- (50) Xu, W.; Wang, M.; Ma, Z.; Shan, Z.; Li, C.; Wang, H. Selenophene-Based Heteroacenes: Synthesis, Structures, and Physicochemical Behaviors. *J. Org. Chem.* **2018**, 83, 12154–12163.
- (51) Ashraf, R. S.; Meager, I.; Nikolka, M.; Kirkus, M.; Planells, M.; Schroeder, B. C.; Holliday, S.; Hurhangee, M.; Nielsen, C. B.; Sirringhaus, H.; McCulloch, I. Chalcogenophene Comonomer Comparison in Small Band Gap Diketopyrrolopyrrole-Based Conjugated Polymers for High-Performing Field-Effect Transistors and Organic Solar Cells. *J. Am. Chem. Soc.* **2015**, 137, 1314–1321.
- (52) Dubinina, G. G.; Price, R. S.; Abboud, K. A.; Wicks, G.; Wnuk, P.; Stepanenko, Y.; Drobizhev, M.; Rebane, A.; Schanze, K. S. Phenylene Vinylene Platinum(II) Acetylides with Prodigious Two-Photon Absorption. *J. Am. Chem. Soc.* **2012**, 134, 19346–19349.
- (53) Li, Z.; Cui, P.; Wang, C.; Kilina, S.; Sun, W. Nonlinear Absorbing Cationic Bipyridyl Iridium(III) Complexes Bearing Cyclometalating Ligands with Different Degrees of π -Conjugation: Synthesis, Photophysics, and Reverse Saturable Absorption. *J. Phys. Chem. C* **2014**, 118, 28764–28775.
- (54) Iqbal, A.; Jost, M.; Kirchmayr, R.; Pfenninger, J. A.; Rochat, A.; Wallquist, O. The Synthesis and Properties of 1,4-diketopyrrolo[3,4-C]pyrroles. *Bull. Soc. Chim. Belg.* **1988**, 97, 615–643.
- (55) Shahid, M.; Thomas, M. W.; John, L.; Stephan, R.; Ester, B. D.; Scott, E. W.; Natalie, S.; Thomas, D. A.; Martin, H. Low Band Gap Selenophene–Diketopyrrolopyrrole Polymers Exhibiting High and Balanced Ambipolar Performance in Bottom-Gate Transistors. *Chem. Sci.* **2012**, 3, 181–185.
- (56) Kumar, C. H. P.; Ganesh, K.; Suresh, T.; Sharma, A.; Bhanuprakash, K.; Sharma, G. D.; Chandrasekharan, M. Influence of Thermal and Solvent Annealing on the Morphology and Photovoltaic Performance of Solution Processed, D–A–D Type Small Molecule Based Bulk Heterojunction Solar Cells. *RSC Adv.* **2015**, 5, 93579–93590.
- (57) Cai, Y.; Liang, P.; Si, W.; Zhao, B.; Shao, J.; Huang, W.; Zhang, Y.; Zhang, Q.; Dong, X. A Selenophene Substituted Diketopyrrolopyrrole Nanotheranostic Agent for Highly Efficient Photoacoustic/Infrared-Thermal Imaging-Guided Phototherapy. *Org. Chem. Front.* **2018**, 5, 98–105.
- (58) Cuesta, V.; Vartanian, M.; Malhotra, P.; Biswas, S.; de la Cruz, P.; Sharma, G. D.; Langa, F. Increase in Efficiency on Using Selenophene Instead of Thiophene in π -Bridges for D- π -DPP- π -D Organic Solar Cells. *J. Mater. Chem. A* **2019**, 7, 11886–11894.
- (59) Cuesta, V.; Vartanian, M.; Cruz, P. D.; Singhal, R.; Sharma, G. D.; Langa, F. Comparative Study on the Photovoltaic Characteristics of A–D–A and D–A–D Molecules Based on Zn-Porphyrin; a D–A–D Molecule with Over 8.0% Efficiency. *J. Mater. Chem. A* **2017**, 5, 1057–1065.
- (60) Loser, S.; Bruns, C. J.; Miyauchi, H.; Ortiz, R. P.; Facchetti, A.; Stupp, S. I.; Marks, T. J. A Naphthodithiophene-Diketopyrrolopyrrole Donor Molecule for Efficient Solution-Processed Solar Cells. *J. Am. Chem. Soc.* **2011**, 133, 8142–8145.
- (61) Strachan, J.-P.; Gentemann, S.; Seth, J.; Kalsbeck, W. A.; Lindsey, J. S.; Holtz, D.; Bocian, D. F. Effects of Orbital Ordering on Electronic Communication in Multiporphyrin Arrays. *J. Am. Chem. Soc.* **1997**, 119, 11191–11201.
- (62) Frisch, M. J.; Trucks, G. W.; Schlegel, H. B.; Scuseria, G. E.; Robb, M. A.; Cheeseman, J. R.; Scalmani, G.; Barone, V.; Petersson, G. A.; Nakatsuji, H.; et al. *Gaussian 16*, Rev. C.01; Wallingford CT, 2016.
- (63) Perdew, J. P.; Burke, K.; Ernzerhof, M. Generalized Gradient Approximation Made Simple. *Phys. Rev. Lett.* **1996**, 77, 3865–3868.
- (64) Hay, P. J.; Wadt, W. R. Ab Initio Effective Core Potentials for Molecular Calculations. Potentials for the Transition Metal Atoms Sc to Hg. *J. Chem. Phys.* **1985**, 82, 270–283.
- (65) Wadt, W. R.; Hay, P. J. Ab Initio Effective Core Potentials for Molecular Calculations. Potentials for Main Group Elements Na to Bi. *J. Chem. Phys.* **1985**, 82, 284–298.
- (66) Francl, M. M.; Pietro, W. J.; Hehre, W. J.; Binkley, J. S.; Gordon, M. S.; DeFrees, D. J.; Pople, J. A. Self-Consistent Molecular Orbital Methods. XXIII. A Polarization-Type Basis Set for Second-Row Elements. *J. Chem. Phys.* **1982**, 77, 3654–3665.
- (67) Cossi, M.; Barone, V.; Cammi, R.; Tomasi, J. Ab Initio Study of Solvated Molecules: A New Implementation of The Polarizable Continuum Model. *Chem. Phys. Lett.* **1996**, 255, 327–335.
- (68) Barone, V.; Cossi, M.; Tomasi, J. Geometry Optimization of Molecular Structures in Solution by the Polarizable Continuum Model. *J. Comput. Chem.* **1998**, 19, 404–417.
- (69) Benkyi, I.; Tapavicza, E.; Fliegl, H.; Sundholm, D. Calculation of Vibrationally Resolved Absorption Spectra of Acenes and Pyrene. *Phys. Chem. Chem. Phys.* **2019**, 21, 21094–21103.
- (70) Santoro, F.; Improta, R.; Lami, A.; Bloino, J.; Barone, V. Effective Method to Compute Franck-Condon Integrals for Optical Spectra of Large Molecules in Solution. *J. Chem. Phys.* **2007**, 126, 084509.
- (71) Barone, V.; Bloino, J.; Biczysko, M.; Santoro, F. Fully Integrated Approach to Compute Vibrationally Resolved Optical Spectra: From Small Molecules to Macrosystems. *J. Chem. Theory Comput.* **2009**, 9, 540–554.
- (72) Furche, F.; Ahlrichs, R. Adiabatic Time-Dependent Density Functional Methods for Excited State Properties. *J. Chem. Phys.* **2002**, 117, 7433–7447.
- (73) Van Caillie, C.; Amos, R. D. Geometric Derivatives of Density Functional Theory Excitation Energies Using Gradient-Corrected Functionals. *Chem. Phys. Lett.* **2000**, 317, 159–164.
- (74) Martin, R. L. Natural Transition Orbitals. *J. Chem. Phys.* **2003**, 118, 4775–4777.

- (75) Humphrey, W.; Dalke, A.; Schulten, K. VMD: Visual Molecular Dynamics. *J. Mol. Graphics* **1996**, *14*, 33–38.
- (76) Lv, B.; Shen, X.; Xiao, J.; Duan, J.; Wang, X.; Yi, Y. Synthesis, Single Crystal, and Physical Properties of Asymmetrical Thiophene/Selenophene-Fused Twistacenes. *Chem. Asian J.* **2015**, *10*, 2677–2682.
- (77) Englman, R.; Jortner, J. The Energy Gap Law for Radiationless Transitions in Large Molecules. *Mol. Phys.* **1970**, *18*, 145–164.
- (78) Mei, J.; Leung, N. L. C.; Kwok, R. T. K.; Lam, J. W. Y.; Tang, B. Z. Aggregation-Induced Emission: Together We Shine, United We Soar! *Chem. Rev.* **2015**, *115*, 11718–11940.